Bioactive Materials 18 (2022) 72–90

Contents lists available at ScienceDirect

Bioactive Materials

journal homepage: www.keaipublishing.com/en/journals/bioactive-materials

Cubic multi-ions-doped Na_2TiO_3 nanorod-like coatings: Structure-stable, highly efficient platform for ions-exchanged release to immunomodulatory promotion on vascularized bone apposition

Dongmei Yu [a,1], Bo Li [a,1], Meng Yu [a,1], Shuo Guo [b], Zheng Guo [b,**], Yong Han [a,*,1]

[a] State Key Laboratory for Mechanical Behavior of Materials, Xi'an Jiaotong University, Xi'an, 710049, Shaanxi, China
[b] Department of Orthopaedics, Tangdu Hospital, Fourth Military Medical University, Xi'an, 710038, Shaanxi, China

ARTICLE INFO

Keywords:
Nanorod-like coating
Ion doping
Sodium titanate
Immunomodulation
Angiogenesis
Osseointegration

ABSTRACT

The dissolution-derived release of bioactive ions from ceramic coatings on metallic implants, despite improving osseointegration, renders a concern on the interfacial breakdown of the metal/coating/bone system during long-term service. Consequently, persistent efforts to seek alternative strategies instead of dissolution-derived activation are pressingly carrying out. Inspired by bone mineral containing ions as Ca^{2+}, Mg^{2+}, Sr^{2+} and Zn^{2+}, here we hydrothermally grew the quadruple ions co-doped Na_2TiO_3 nanorod-like coatings. The co-doped ions partially substitute Na^+ in Na_2TiO_3, and can be efficiently released from cubic lattice via exchange with Na^+ in fluid rather than dissolution, endowing the coatings superior long-term stability of structure and bond strength. Regulated by the coatings-conditioned extracellular ions, TLR4-NFκB signalling is enhanced to act primarily in macrophages (MΦs) at 6 h while CaSR-PI3K-Akt1 signalling is potentiated to act predominately since 24 h, triggering MΦs in a M1 response early and then in a M2 response to sequentially secrete diverse cytokines. Acting on endothelial and mesenchymal stem cells with the released ions and cytokines, the immunomodulatory coatings greatly promote Type-H ($CD31^{hi}Emcn^{hi}$) angiogenesis and osteogenesis *in vitro* and *in vivo*, providing new insights into orchestrating insoluble ceramics-coated implants for early vascularized osseointegration in combination with long-term fixation to bone.

1. Introduction

A prerequisite for endosseous implants to function is fixation to host bone by integration, which is required as early as possible [1,2]. Osseointegration of implants is formed via inducing *de novo* bone apposition on their surfaces [3]. It is now recognized that *de novo* bone apposition involves in the participation of diverse cells, such as immune cells — primarily macrophages (MΦs) that may polarize towards a pro-inflammatory (M1) or a pro-healing (M2) phenotype, endothelial cells (ECs) and mesenchymal stem cells (MSCs), but also the interplay of the cells via paracrine cytokines [4]. Specially, MΦs-secreted cytokines, such as pro/anti-inflammatory and angio/osteo-genic factors, are given to dominantly affect the activity of the other cells [4,5]. Osseointegration is initiated principally by MΦs-derived inflammatory response to implants, followed by M1-to-M2 transition, angio- and osteo-genesis in a temporal sequence [6–8]. ECs-assembled blood vessels precede osteogenesis, controlling it by delivering oxygen, nutrients, ions and angiokines but also by bringing selectively positioned MSCs [9–11]. Blood vessels in bone are functionally specialized, while postnatal bone capillaries have two subtypes: a small subset of type-H, in which ECs express highly positive CD31 and endomucin ($CD31^{hi}Emcn^{hi}$), and type-L, in which ECs show low levels of CD31 and Emcn ($CD31^{lo}Emcn^{lo}$) [12]. Notably, the perivascular MSCs selectively position around type-H but not type-L capillaries, and type-H ECs provide angiokines to act on MSCs and to couple angiogenesis and osteogenesis [12]. Reportedly, prolonged inflammation delays angiogenesis and osteogenesis [8], early M1-to-M2 shift at the bone-implant interface can mitigate inflammation and improve osseointegration [6], and implant materials can be

Peer review under responsibility of KeAi Communications Co., Ltd.

* Corresponding author.
** Corresponding author.
E-mail addresses: guozheng@fmmu.edu.cn (Z. Guo), yonghan@mail.xjtu.edu.cn (Y. Han).

[1] Co-first authors: These authors contributed equally to this work.

https://doi.org/10.1016/j.bioactmat.2022.01.039
Received 20 December 2021; Received in revised form 10 January 2022; Accepted 22 January 2022
Available online 15 February 2022

endowed local immunomodulatory function via regulating their surface features (such as chemical constituent, topography and hydrophilicity) [4,5]. Therefore, timely termination of inflammation by M1-to-M2 shift and angiogenesis especially for Type-H using immunomodulatory materials are critical to early osseointegration.

The fixation of joint/dental implants to bone should be firm enough and lifelong lasting [1,2]. For a metallic implant, which usually exhibits intervening fibrous capsule *in vivo*, adding a layer of ceramics such as calcium phosphate (CaP) and calcium silicate (CaSi) to its surface is shown to improve osseointegration, while incorporation of other ions (e.g. Mg^{2+}, Sr^{2+} and Zn^{2+}) into them further promotes osseointegration [2,13,14]. Clearly, the bioactivity of these ceramics is contributed to the release of Ca^{2+}, PO_4^{3-}, SiO_3^{2-} and the doped-ions via dissolution, and more soluble coatings promote osseointegration more earlier [1,2,13,14]. However, such soluble nature of the ceramics renders a concern on interfacial bonding breakdown of the metal/ceramic/bone system during long-term service, which results not only from the delamination of coating owing to its decreased cohesive and adhesive strength, also from the complete dissolution of coating to expose substrate [2,15]. To solve the conflict between early osseointegration and long-term fixation of the soluble ceramics coated implants to bone, persistent efforts to seek alternative strategies instead of dissolution-derived activation are currently carrying out. Especially, boron nitride [16] as well as nanostructured titania [17] and hydrogen titanates [18], all being insoluble, have been recently developed to act respectively as hydrophilic activation and topographic activation of metal implants, drawing a paradigm for activation without dissolution of coatings.

Besides CaP, CaSi and their ions-doped derivants, perovskite $MTiO_3$ (M = Sr, Ca, Mg or Zn) nanostructured coatings, formed by hydrothermal growth reaction [19–21] or by ion exchange [22,23], also release bioactive ions but quite less via the subtle dissolution of $MTiO_3$ [19,24]. This subtle dissolution still arises a worry about the lifelong structure stability of $MTiO_3$ coatings [19]. Alternatively, bioactive ions are proven to be released from M^{2+}-doped sodium hydrogen titanate ($Na_xH_{2-x}Ti_yO_{2y+1}$) [25–29] and sodium titanate ($Na_2Ti_yO_{2y+1}$) [30–33] nanostructured coatings. In the works [25–33], Na^+ ions, which locate at the interlayers between TiO_6 octahedral slabs of $Na_xH_{2-x}Ti_yO_{2y+1}$ and $Na_2Ti_yO_{2y+1}$, are entirely substituted by one or two types of M^{2+} ions, and the resultant derivatives still keep monoclinic structure. The release of M^{2+} ions from the entirely doped $Na_xH_{2-x}Ti_yO_{2y+1}$ is considered to carry out via ion exchange with H_3O^+ in simulated body fluid (SBF) [25,26,29]. However, the mechanism by which M^{2+} ions are released from the entirely doped $Na_2Ti_yO_{2y+1}$ has not been elucidated [30–33]; even controversially, most of M^{2+} ions are permanently trapped in the doped $Na_2Ti_yO_{2y+1}$ lattice, unable to be released out through ion exchange [34].

Growing evidence supports a further enhanced role of the released ions in bio-activation on the basis of nanostructures. Although current literature only achieves the incorporation of one or two kinds of Ca^{2+}, Mg^{2+}, Sr^{2+} and Zn^{2+} ions into nanostructured titanate coatings, these doped coatings are shown to promote the adhesion, proliferation, osteodifferentiation of MSCs or extracellular matrix (ECM) mineralization [20,27,30–33] as well as osseointegration [27,33], compared to the corresponding un-doped ones. Moreover, each kind of the released ions shows the ability to switch MΦs to M2 phenotype in a dose-dependent manner [21,33,35], and the co-release of Sr^{2+} and Ca^{2+} enhances the switch than either of them [36].

Inspired by the bone mineral containing multi-ions as trace Mg^{2+}, Sr^{2+} and Zn^{2+} besides primary Ca^{2+} [37], herein we fabricated Ca^{2+}, Mg^{2+}, Sr^{2+} and Zn^{2+} co-doped sodium titanate (ST, Na_2TiO_3) nanorods arrayed coatings on Ti using hydrothermal method. The quadruple ions co-doped ST is cubic in crystallography, different from the monoclinic phase of M^{2+}-doped $Na_xH_{2-x}Ti_yO_{2y+1}$ and $Na_2Ti_yO_{2y+1}$ [25–33], showing much higher total release dose of the co-doped ions than the currently reported. The ionic release is identified to carry out via exchange of the doped ions with Na^+ in fluid rather than dissolution, endowing the co-doped ST coatings superior stability of structure and bond strength. We also show that the quadruple ions co-doped ST coatings favor to polarize MΦs towards M1 phenotype followed by M1-to-M2 shift, and promote Type-H angiogenesis and osteogenesis *in vitro* and *in vivo*, providing new insights into orchestrating early osseointegration in combination with long-term fixation for insoluble ceramics-coated implants.

2. Experimental section

2.1. Preparation and **multi-ionic** incorporation of sodium titanate nanorods arrayed coating

Commercially pure titanium (Ti) were machined into disks (Ø 14 × 2 mm) and screws (M1.7 × 4 mm), followed by cleaning successively with acetone, ethanol and distilled water. For the formation of sodium titanate (ST) nanorods, each of Ti disks and screws was mounted in a Teflon-lined autoclave and hydrothermally treated firstly in 10 mL of 1 M NaOH aqueous solution at 100 °C keeping 1.5 h for ST nucleation, and alternatively in 10 mL of 0.5 M NaOH aqueous solution at 220 °C lasting 4 h for topographical ST growth. For incorporation of multi-ions, the ST coated samples were mounted in autoclaves containing aqueous solutions with three kinds of concentrations of magnesium-, calcium-, strontium- and zinc acetate (Table S1, supporting information (SI)) and treated at 100 °C for 24 h, while the resultant dual-ions (Ca^{2+} and Mg^{2+}) and quadruple-ions (Ca^{2+}, Mg^{2+}, Sr^{2+} and Zn^{2+}) co-doped ST were referred to as DID, 1QID and 2QID, respectively.

2.2. Structure characterization of the coatings

The coatings' morphologies and compositions were examined using a scanning electron microscope (SEM; JEOL JSM-6700F, Japan) equipped with an energy dispersive X-ray spectrometer (EDX) operating at 20 kV. The geomorphological parameters of the nanorods, including interrod spacing, rod diameter and length, were examined with Image J (Pawak Incorporation, Germany) from surface and cross-sectional SEM images. Five random areas were measured to get the average values. Phasic components were identified with an X-ray diffractometer (XRD; X'Pert PRO, Netherland) using a Cu Kα irradiation at an accelerating voltage of 40 kV, an incident angle of 0.5° and a scanning speed of 8° min^{-1}. The nanorods scratched from the coatings were examined with a transmission electron microscope (TEM; JEM-2100F, JEOL, Japan) operating at 200 kV and the nanorod elements were conducted using the TEM-equipped EDX (JEOL, Japan) under the scanning transmission electron microscope (STEM) model, respectively. The chemical species of the coatings were detected using an X-ray photoelectron spectroscope (XPS; Thermo Electron Corporation, USA), with an Al Kα radiation line as the X-ray source and take-off angle of 45°, taking C1s peak at 284.6 eV as an internal reference for calibrating peak positions.

2.3. Roughness, hydrophilicity, ion release profiles as well as structural and bond strength stability of the coatings

The surface roughness and hydrophilicity of each kind of the coated and bare Ti discs were measured using an atomic force microscope (AFM; Edge, Bruker, American) and a contact angle device (DSA30, Kruss, Germany) for triplicate, respectively. During each hydrophilicity test, a 2 μL droplet of distilled water was applied to a disc and the droplet-to-disc contact was collected with a camera.

The bare and coated Ti discs were respectively immersed in 1 mL of physiological saline (PS) and Dulbecco's modified Eagle's medium (DMEM) at 37 °C for a series of periods without refreshing during immersion. The discs-immersed solutions were picked up to detect their pH values with a digital pH meter and ionic concentrations using an inductively coupled plasma-mass spectrometry (ICP-MS; Agilent 7700, USA), respectively, and the pH and ion release tests were performed on

five replicates for each kind of the discs-immersed solutions at each time point. In addition, the morphologies and compositions of the immersed coatings and especially nanorods were also examined using SEM and TEM both equipped with EDX, respectively. The arrays coated discs were respectively immersed in 50 mL of SBF with refreshing every two days, and SEM observed for CaP precipitation. The pristine concentrations and pH of PS, DMEM and SBF are listed in Table S2 (SI). Furthermore, the bond strengths of the pristine and immersed coatings were assessed using a scratch tester (WS-2005, China). The scratch critical load, **i.e.**, the smallest load at which a recognizable failure occurred, was drawn from the load versus acoustic output curve together with SEM and EDX examinations of the scratch, and averaged by three replicates for each coating.

2.4. In vitro cell response to the coated and bare Ti discs

2.4.1. The used cells and their culture

The used cells for testing the coated and bare discs were MΦs—murine-derived cell line RAW 264.7, rat bone marrow-derived mesenchymal stem cells (rBMSCs), both from Chinese Academy of Sciences, and human umbilical vein endothelial cells (HUVECs) from the American Type Culture Collection. MΦs were cultured with DMEM (HyClone, USA) containing 10% fetal bovine serum (FBS; Gibco, USA) and 1% (v/v) penicillin/streptomycin (PN/SN; Gibco, USA). HUVECs were cultured using the medium of endothelial cell (EC) supplemented with 5% FBS, 1% EC growth supplement and 1% PN/SN (ScienCell, USA). rBMSCs were cultured using DMEM/nutrient mixture F-12 Ham (HyClone, USA) supplemented with 10% FBS and 1% PN/SN. These cells were placed into culture dishes, followed by incubation in atmosphere of 95% humidity and 5% CO_2 at 37 °C with refreshing the culture media every two days.

2.4.2. Behavior of MΦs seeded on the coated and bare Ti discs

Subjected to sterilization, the tested discs were placed in 24-well tissue culture plates (TCPs), subsequently MΦs were seeded on each disc at a density of 2×10^4 cells mL^{-1} and incubated for 1, 3 and 7 days. Thereafter, following the successive procedures of fixation in 2.5% glutaraldehyde, dehydration in gradient ethanol, dry and coating gold, MΦs on the discs were observed with SEM. Moreover, FAK100 kit (Millipore, USA) were applied for vinculin, actin and nuclei visualization of MΦs on the discs. Operatively in brief, the MΦs-incubated discs were fixed with 4% paraformaldehyde (PFA), permeabilized with 0.1% Triton™ X-100 (Sigma, USA) and washed three times using PBS containing 0.05% Tween®20 (Sigma, USA). Thereafter, the cells were incubated with 1% bovine serum albumin (BSA; Sigma, USA) at room temperature (RT) for 30 min and further incubated with the anti-vinculin primary antibody at RT for 2 h, followed by washing triple with PBS containing 0.05% Tween®20; then the fluorescent secondary antibody Alexa Fluor 594 (Thermo Scientific, USA) and FITC-labeled phalloidin were applied for 1 h to visualize vinculin and actin, respectively, followed by 4, 6-diamidino-2-phenylindole (DAPI) to stain nuclei. The staining images were collected using a laser scanning confocal microscope (LSCM; FV1000, Olympus, Japan).

For CC-chemokine receptor-7 (CCR-7) and arginase-1 (Arg-1) of MΦs incubated on the discs, their mRNA expressions were examined using a quantitative real-time polymerase chain reaction (qRT-PCR), and normalized to the housekeeping gene, glyceraldehyde-3-phosphate dehydrogenase (GAPDH). The sequences of the involved gene primers are listed in Table S3 (SI). To examine CCR-7 and Arg-1 at protein level, the MΦs on the discs were successively fixed with 4% PFA, permeabilized with 0.1% Triton™ X-100, blocked with 1% BSA, and incubated with anti-CCR-7 and anti-Arg-1 (Abcam, UK) primary antibodies at 4 °C overnight, followed by washing triple with PBS. Thereafter, DyLight 488 Goat Anti-rabbit IgG (Boster, China) and DyLight 594 Rabbit Anti-mouse IgG (Boster, China) were applied to the cells at RT for 1 h to respectively visualize CCR-7 and Arg-1, followed with DAPI (Servicebio, China) to stain nuclei. The staining images of six random areas per disc were taken using LSCM and the numbers of positively stained cells were counted using Image Pro Plus 6.0 (Media Cybernetics, USA). Furthermore, tumor necrosis factor α (TNF-α), interleukin 1β (IL-1β), IL-4, IL-10, vascular endothelial growth factor A (VEGF-A), platelet-derived growth factor-BB (PDGF-BB), angiopoietin-1 (ANG1), transforming growth factor β1 (TGF-β1), bone morphogenetic protein-2 (BMP2) and stromal-cell-derived factor (SDF-1) secreted by MΦs on the discs were detected by the enzyme-linked immunosorbent assay (ELISA) kits (Thermo Scientific, USA).

Fluorescence staining was employed to examine intracellular Ca^{2+} concentration ($[Ca^{2+}]_i$) of MΦs on the tested discs. Followed by washing triple with PBS, the MΦs-incubated discs were stained in 300 μL PBS containing 5 μM Flour-4 AM (Invitrogen ™, USA) at 37 °C for 30 min then washed twice with PBS. Subsequently, the MΦs-incubated discs were mounted in a confocal vessel containing 1 mL fresh culture medium of MΦs and observed using LSCM to capture fluorescence image and record fluorescence intensity. The fluorescence intensity of each stained cell is positively relative to its $[Ca^{2+}]_i$. The fluorescence intensities of at least 20 MΦs on each kind of discs were recorded to obtain the average.

Western blot was conducted on MΦs on the discs to quantify protein levels of Toll-like receptor 4 (TLR4), IκB kinase α (IKKα), nuclear factor κB p65 (NFκB p65), phosphorylated NFκB p65 (*p*-NFκB p65), Ca^{2+}-sensing receptor (CaSR), phosphatidylinositol-3-kinase (PI3K), phosphorylated Akt1 (*p*-Akt1) and Akt1. Briefly, MΦs cultured for 6 and 24 h were lysed with RIPA buffer (Beyotime, China), and the total proteins were quantified with a BCA protein assay kit (Thermo Fisher Scientific, USA). Protein samples were denatured and resolved by sodium dodecyl sulfate-polyacrylamide gel electrophoresis (SDS-PAGE), then transferred onto PVDF membranes (Bio-rad, USA). Such membranes were blocked in tris-buffer saline-T (0.1% Tween 20, TBST) containing 5% BSA, and incubated with primary antibodies anti-TLR4, anti-IKKα, anti-phospho-NFκB p65 (Ser536), anti-NFκB p65, anti-CaSR, anti-PI3K, anti-phospho-Akt1 (Ser 473), anti-Akt1 and GAPDH (CST, USA) at 4 °C overnight, followed by rinsing with TBST. Thereafter, the membranes were incubated with horseradish peroxidase-conjugated secondary antibodies (anti-Rabbit or anti-Mouse, Beyotime, China) at RT for 1 h, followed by rinsing with TBST five times. Next, the membranes containing protein bands were visualized by ECL substrate (Millipore, USA) under ChemiDoc Touch Imaging Systems (Bio-rad, USA). The results were quantified using Image J software (NIH, USA), normalized with GAPDH.

2.4.3. Co-culture of HUVECs/rBMSCs with MΦs on the coated and bare Ti discs

After seeding MΦs at a density of 2×10^4 cells mL^{-1} onto the discs mounted in 24-well TCPs, a transwell chamber with a permeable pore size of 8 μm (Thermo Scientific, USA) was placed above each well, and HUVECs were then seeded onto the upper side of transwell permeable membrane (TPM) at a density of 2×10^4 cells mL^{-1} to construct a co-culture system of HUVECs and MΦs. Likewise, a co-culture system of rBMSCs and MΦs was also set up by rBMSCs instead of HUVECs.

Post a period of co-culture, the HUVECs recruited on the bottom side of TPM were fixed in 4% PFA and stained with crystal violet (Sigma, USA), followed by observation using an inverted light microscope (DM1000, Leica, Germany) to assay their migrating abilities across TPM, and so did the rBMSCs recruited on the bottom side of TPM.

Following co-culture for diverse durations, the mRNA expression of hypoxia-inducible factor (HIF-1α), VEGF-A and PDGF-BB by the recruited HUVECs were assayed with RT-qPCR and normalized to GAPDH, in which the sequences of the involved gene primers were listed in Table S3 (SI). After lysing the recruited HUVECs with 0.2% Triton-X 100, centrifuging and harvesting the supernatant, the intracellular HIF-1α protein was assessed using EHC080 ELISA kit (NeoBioscience, China). The recruited HUVECs-secreted VEGF-A, PDGF-BB, and BMP2

were detected using ELISA kits (Thermo Scientific, USA). The tubular assemble of the HUVECs recruited onto TPM bottom side was visualized using an inverted light microscope (DM1000, Leica, Germany) after washing with PBS and fixing with 2.5% glutaraldehyde. The total tubular length and branch point were counted within randomly selected five visualized-fields using Image pro plus software. To identify the subtype of the recruited HUVECs assembled tubules, the platelet endothelial cell adhesion molecule-31 (CD31) and Endomucin (Emcn) were assayed at protein level with fluorescence staining. In details, the recruited HUVECs were orderly fixed with 4% PFA, permeabilized with 0.1% Triton™ X-100, blocked with 1% BSA, and double-stained with anti-CD31 (Abcam, UK) and anti-Emcn (Affinity Biosciences, USA) primary antibodies at 4 °C overnight, followed by washing with PBS. Thereafter, DyLight 488 Goat Anti-mouse IgG (Boster, China) and DyLight 594 Goat Anti-rabbit IgG (Boster, China) were applied to the cells at RT for 1 h to respectively visualize CD31 and Emcn, followed by staining nuclei with DAPI (Servicebio, China). The next image collection and analysis were carried out identically to those mentioned on CCR-7 and Arg-1.

Also, the mRNA expressions of HIF-1α, VEGF-A, PDGF-BB, Runt-related transcription factor 2 (Runx2), osteopontin (OPN), and osteocalcin (OCN) by the recruited rBMSCs were assayed using RT-qPCR and normalized to GAPDH, with the sequences of the involved gene primers listed in Table S3 (SI). The intracellular HIF-1α protein of the recruited rBMSCs was assessed using CSB-E08540r ELISA kit (CUSABIO, China) after lysing the cells, centrifuging and harvesting the supernatant. The recruited rBMSCs-secreted VEGF-A, PDGF-BB and BMP2 were detected by ELISA kits (Thermo Scientific, USA). To evaluate alkaline phosphatase (ALP) activity and ECM mineralization, the recruited rBMSCs were fixed in 4% PFA, then stained with ALP staining kit (Abcam, UK) and alizarin red staining kit (Servicebio, China), respectively, followed by observation using a Leica DM1000 inverted light microscope.

2.4.4. Mono-culture of HUVECs/rBMSCs in response to ions released from the coatings

Correspondingly, mono-culture of HUVECs/rBMSCs were likewise performed in a transwell manner described in the aforementioned co-culture case but on the underlying discs without seeding MΦs. Post a period of mono-culture, diverse cytokine expressions at mRNA and protein levels by the HUVECs/rBMSCs recruited on the bottom side of TPM were examined using the same method described in section 2.4.3.

2.5. In vivo implantation tests of the coated and bare Ti screws

Male Sprague-Dawley (SD) rats (eight weeks old and 200 g weight), supplied by Animal Resource Center, Fourth Military Medical University, were employed for implantation of the screws. All the animal test procedures have been approved by the Ethics Committee of Fourth Military Medical University. Briefly, seventy-five rats were randomly divided into five groups to implant the coated and bare Ti screws. Following anesthesia of the rats by an intraperitoneal injection of pentobarbital sodium solution, drilling a hole (Ø 1.5 × 4 mm) on each of the both hind limb femoral condyles of a rat, the screws were processed into the holes followed by suturing and smearing the wounds with erythromycin ointment. In this procedure, for each kind of the screws at each implantation period, six samples and three rats were employed in the implantation manner of one screw per femoral condyle. After surgery, all the rats received an intramuscular injection of penicillin 80 thousand units day^{-1} for 3 days to prevent infection, and normal dietary intake.

After sacrificing the rats at a series of implantation periods, the screws-implanted femoral condyles were picked up, followed by fixation in 4% PFA, decalcification in 10% EDTA solution for 21 days, removal of the screws, dehydration in ethanol and embedment into paraffin, and then cut into thin sections with a thickness of 5 μm using a cutting-unit (Leica, Germany). Diverse fluorescence staining examinations were performed on the thin sections, especially focusing on the regions adjacent to the tissue-implant interfaces. These examinations included cellular identifications, such as MΦ phenotypic makers CCR-7 and Arg-1 stained respectively with anti-CCR7 and anti- Arg-1 antibodies, EC indicatives CD31 and Emcn stained respectively with anti-CD31 and anti-Emcn antibodies, MSC indicative CD90 stained with anti-CD90/Thy1 antibody (Abcam, UK), and collagen-1 (Col-1) and OPN as indicatives of MSC osteogenic differentiation stained respectively with anti-collagen I rabbit pAb and anti-osteopontin rabbit pAb (Servicebio, China), and cellular nuclei stained with DAPI (Servicebio, China). In addition, hematoxylin-eosin (HE) staining and Masson staining of the thin sections were performed with HE dye solution set and Masson dye solution set (Servicebio, China) for tissue identification. The straining images were collected with a Pannoramic scanner (250/MIDI, 3D HISTECH, Hungary) and quantitative analyses were undertaken using Image-Pro Plus software 6.0.

The screws-contained femoral condyles retrieved post implantation of 2 and 4 weeks, on one hand were examined for new bone volume using micro computed tomography (micro-CT, Yxlon International GmbH, Y. Cheetah, Germany) at an applied voltage of 90 kV, current of 50 μA and scanning resolution of 7 μm, on the other hand were histologically examined. To this end, they were fixed in 4% PFA, dehydrated in ethanol, embedded with polymethyl methacrylate, and cut into ~150 μm thick sections with a Leitz1600 microtome (Hamburg, Germany). The thick sections were ground, polished to foils (~50 μm in thickness) and then stained with Van Gieson's (VG) picric–fuchsine. The stained foils were pictured with an optical microscope (Olympus IX 71, Japan), and the bone–to–implant contact ratio for each kind of the screws was quantified using Image-Pro Plus software 6.0 based on the images taken from three stained foils (five images per foil).

2.6. Statistical analysis

The results were expressed as mean ± standard deviation. The data were analyzed using SPSS 19.0 software (SPSS, USA). A one-way ANOVA followed by a Student-Newman-Keuls post hoc test was used to determine the level of significance: $p < 0.05$ and 0.01 was considered to be significant and highly significant, respectively.

3. Results and discussion

3.1. Structures, ionic release and bond strengths of ions-doped nanorods arrayed coatings

The coating, hydrothermally grown on Ti disc in an autoclave containing NaOH aqueous solution, is bilayer structured, comprising a thin layer of compact nanogranulates adjacent to Ti, and an overlapping layer of quasi-vertically aligned and top-flat nanorods with a nanorod diameter of 65.1 ± 2.5 nm, length of ~2 μm and interrod spacing of 75.4 ± 3.2 nm (Fig. 1a). This coating consists of cubic ST (Na_2TiO_3) (Fig. 1b), with TiO_6 octahedra joining each other and sharing vertices to form slabs while Na^+ ions locating at the voids enclosed by the TiO_6 octahedrons [38]. The nanorods of the coating are stacked in radial direction by TiO_6 octahedral slabs-constructed layers with a growth direction along a-axis [100] (Fig. 1c). Subsequently, we achieved the uniform incorporation of Ca^{2+} and Mg^{2+} dual ions as well as Ca^{2+}, Mg^{2+}, Sr^{2+} and Zn^{2+} quadruple ions into ST nanorods in whole length (Fig. 1d and e) by hydrothermal ion exchange in an autoclave containing the aqueous solution of the doped ions, and the resultant are referred to as DID, 1QID and 2QID. Examined with TEM equipped EDX, Ca^{2+} shows the highest dose among the co-doped ions in each kind of the derivants. DID has a similar Mg^{2+} doping dose and total doping dose of multi-ions to 1QID and a Ca^{2+} doping dose ~2.7-fold of that in 1QID, while 2QID has a doping dose of individual ions ~ twice of that in 1QID (Fig. 1e, i), of which the stoichiometric formulas are presented in Fig. 1i. As known, Ca^{2+} and Sr^{2+} are 0.99 and 1.13 Å in radius [39] larger than Na^+ (0.95

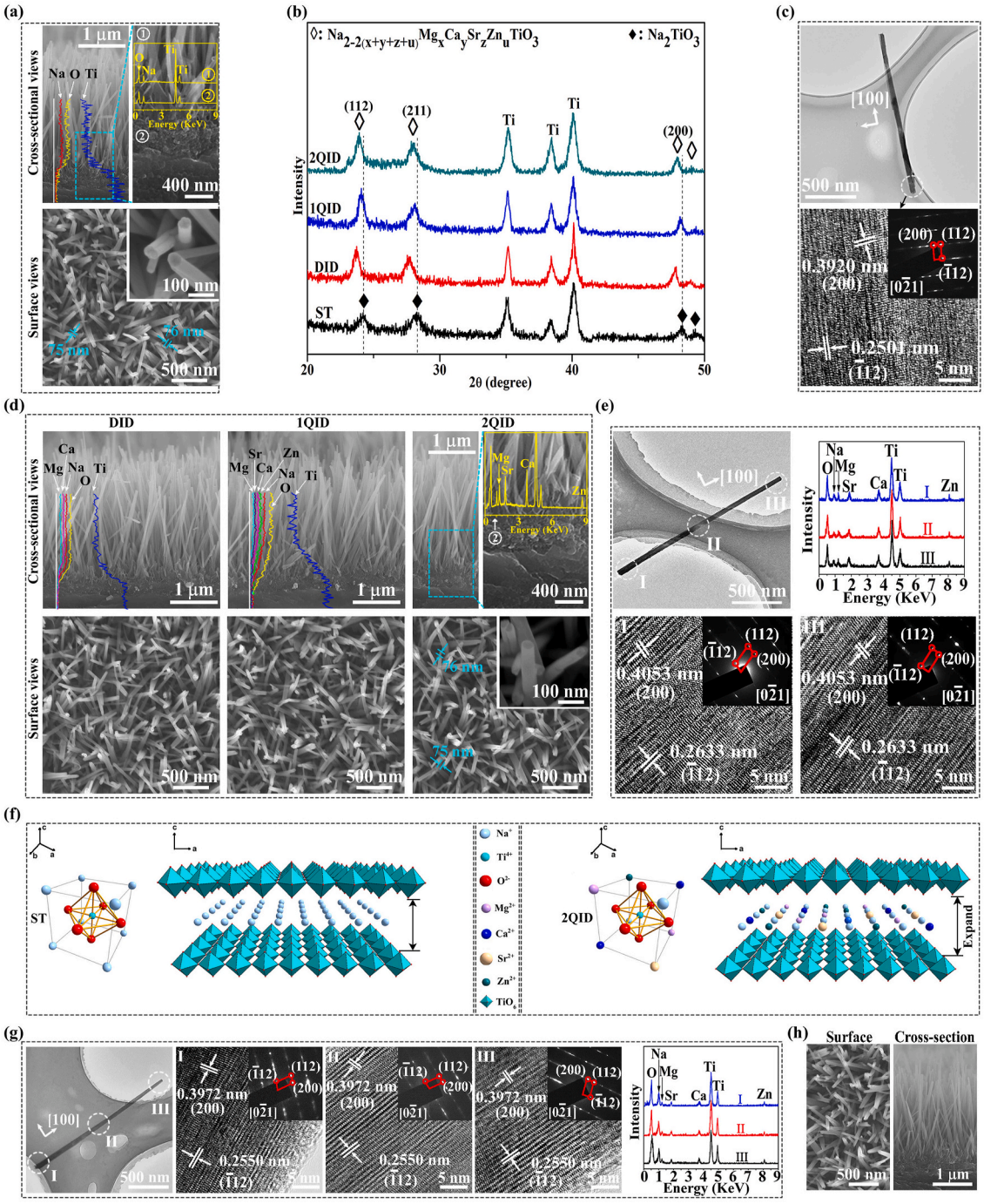

(i)

Terminology		Elemental composition (At. %)							Stoichiometric formula
		Ti	O	Na	Mg	Ca	Sr	Zn	
As-received	ST	16.8±0.7	50.0±0.8	33.2±0.5	—	—	—	—	Na_2TiO_3
	DID	16.8±0.5	50.0±0.8	19.7±0.3	1.7±0.1	11.8±0.2	—	—	$Na_{1.2}Mg_{0.05}Ca_{0.35}TiO_3$
	1QID	16.7±0.6	50.1±0.9	21.8±0.4	1.9±0.1	4.3±0.1	3.8±0.2	1.4±0.1	$Na_{1.30}Mg_{0.06}Ca_{0.13}Sr_{0.12}Zn_{0.04}TiO_3$
	2QID	16.6±0.5	50.2±1.0	10.1±0.4	3.9±0.2	8.6±0.3	7.6±0.2	3.0±0.2	$Na_{0.60}Mg_{0.12}Ca_{0.26}Sr_{0.23}Zn_{0.09}TiO_3$
After immersing	ST	16.7±0.9	50.2±1.2	33.1±0.5	—	—	—	—	$Na_{2-x}H_xTiO_3$
	DID	16.7±0.7	50.2±0.9	26.3±0.2	0.7±0.1	6.1±0.3	—	—	$Na_{1.60}Mg_{0.02}Ca_{0.18}TiO_3$
	1QID	16.6±0.8	50.3±1.0	27.6±0.4	0.9±0.1	2.2±0.1	1.6±0.2	0.8±0.1	$Na_{1.66}Mg_{0.03}Ca_{0.07}Sr_{0.05}Zn_{0.02}TiO_3$
	2QID	16.5±0.8	50.4±1.0	20.7±0.4	1.9±0.2	4.6±0.2	4.2±0.1	1.7±0.2	$Na_{1.24}Mg_{0.06}Ca_{0.14}Sr_{0.13}Zn_{0.05}TiO_3$

(caption on next page)

Fig. 1. (a) SEM pictured cross-sectional and surface images of ST coating, elemental distribution profiles along the cross-section, and magnified image of ST/Ti interfacial structure along with EDX spectra detected on ①-marked nanorods and ②-marked nanogranulates. (b) XRD patterns of ST, DID, 1QID and 2QID coatings. (c) TEM image of the nanorod with an intact length of ~2 μm picked up from ST coating as well as high-resolution TEM (HRTEM) image and inserted selected area electron diffraction (SAED) pattern of the nanorod. (d) Cross-sectional and surface SEM images of DID, 1QID and 2QID coatings, elemental distribution profiles along the cross-sections, and magnified image of 2QID/Ti interfacial structure along with EDX spectrum detected on ②-marked nanogranulates. (e) TEM image of the nanorod with an intact length of ~2 μm picked up from 2QID coating as well as HRTEM images, inserted SAED patterns and EDX spectra taken from I, II and III marked areas on the nanorod. (f) Schematic diagrams of atom stack models of ST and 2QID along with their layered structures. (g) TEM image of a full long nanorod picked up from 2QID coating after immersion in PS solution for 60 d as well as HRTEM images, inserted SAED patterns and EDX spectra taken from I, II and III marked areas on the nanorod. (h) Surface and cross-sectional SEM images of 2QID coating after immersion in PS solution for 60 d. (i) EDX-detected elemental compositions under scanning TEM (STEM) model of TEM and consequently drawn stoichimoteric formulas of the nanorods picked up from the coatings before and after immersion in PS solution for 60 d.

Å) [40], while Mg^{2+} and Zn^{2+} are 0.65 and 0.74 Å in radius [39] smaller than Na^{+}, respectively. The co-incorporation of these ions does not render DID, 1QID and 2QID to change in morphology (Fig. 1d) and cubic phase (Fig. 1b). However, such doping gives rise to lattice distortion and the increase of interplanar distances compared to ST (Fig. 1e *vs* c, also reflected by the shift of XRD peaks to low angles with doping) due to the highest dose of Ca^{2+} among the doped ions. We calculated bond energy according to Coulomb's law, which is shown to be in the order of Na–O < Sr–O < Ca–O < Zn–O < Mg–O « Ti–O. Based on the calculated result, and the confirmed formation of Ca–O, Sr–O, Mg–O and Zn–O bonds by XPS (Fig. S1, SI), TEM and EDX data also indicate that the co-doped ions partially substitute Na^{+} rather than Ti^{4+}, locating at the interlayers between TiO_6 octahedral slabs, as schematically shown in Fig. 1f.

The ionic release profiles of ST, DID, 1QID and 2QID coated Ti discs were assessed together with bare Ti disc as a control by immersing them in PS up to 60 days and cell culture medium, DMEM, up to 2 days, respectively. In PS, the Ti ions released from ST, DID, 1QID and 2QID coated Ti discs were tested to be quite rare with identical amount to those from bare Ti (Fig. 2a_1), indicating that no additional Ti ions are released from the coatings besides from Ti substrates, excluding the soluble possibility of the coatings. However, Na^{+} ions were observed to be released from ST (Fig. 2a_1), in parallel, the pH value of the ST-immersed PS shows a visible increase (Fig. 2a_2), indicating obvious occurrence of the exchange of Na^{+} in ST with H^{+} in PS. This Na^{+}/H^{+} exchange is weak for DID, 1QID and 2QID, identified by the feebly rise in pH of the resultant solutions (Fig. 2a_2). Moreover, Ca^{2+}, Mg^{2+} and Sr^{2+} are highly released (in the order of $Ca^{2+} > Sr^{2+} > Mg^{2+}$) but Zn^{2+} is rarely released from each of 1QID and 2QID, and so do Ca^{2+} and Mg^{2+} from DID (Fig. 2a_3–a_6), leading to a sustained elevation in their concentrations of the resultant solutions with immersion. Based on the doping dose of Mg^{2+} close to Zn^{2+} in 1QID and 2QID, the above-depicted much higher release rate of Mg^{2+} than Zn^{2+} also indicate that the migration of small radial Mg^{2+} is prone to Zn^{2+} in the Ca^{2+}/Sr^{2+}-induced expandable lattice. Mechanistically, the release of the doped ions from DID, 1QID and 2QID was identified to carry out via exchange of the ions with Na^{+} in PS. This is evidenced by that the interplanar distances (Fig. 1g *vs* 1e) and the contents of the doped ions reduce while Na^{+} content elevates in each kind of the nanorods after immersion in PS for 60 days compared to the according primitive one (Fig. 1i). Consequently, the nanotopographic parameters (i.e. nanorod diameter, length and interrod spacing) of each kind of the nanorods keep unchangeable after immersion of 60 days (representatively as Fig. 1h *vs* 1d). In DMEM, Ca^{2+}, Mg^{2+}, Sr^{2+} and Zn^{2+} display similar release profiles to those in PS accordingly from DID, 1QID and 2QID, leading to an elevation in ion concentrations of the resultant media (Fig. 2b_1–b_4). However, this elevation does not induce CaP-like precipitation within DMEM (also on the arrays immersed in SBF up to 5 days, Fig. S2 in SI). Notably, immersion of DID, 1QID and 2QID in DMEM renders the decline in Na^{+} concentrations (Fig. 2b_5) but almost no change in pH of the resultant media (Fig. 2b_6). Collectively, the release of Ca^{2+}, Mg^{2+}, Sr^{2+} and Zn^{2+} from DID, 1QID and 2QID is spontaneously carried out via exchange of the doped ions with Na^{+} rather than H^{+} in DMEM and PS, as schematically shown in Fig. 2c. The spontaneous ion release is deemed to be derived by the ions-induced high lattice distortion energy, while the exchange of the ions in nanorods with Na^{+} in the solutions can reduce lattice distortion, achieving the lowest energy state. Intriguingly, DID, 1QID and particularly 2QID exhibit much higher total release amounts of co-doping ions (Fig. 2d) than the monoclinic M^{2+}-doped $Na_xH_{2-x}Ti_yO_{2y+1}$ and $Na_2Ti_yO_{2y+1}$ [20,26,30–32], providing the cubic ions-doped Na_2TiO_3 that has high symmetry as a highly efficient platform for releasing bioactive ions. The lower ion release profiles of the monoclinic M^{2+}-doped $Na_xH_{2-x}Ti_yO_{2y+1}$ and $Na_2Ti_yO_{2y+1}$ likely ascribes to their low symmetry, making large radial ions difficult to migrate in lattice (exampled as Zn^{2+} *vs* Mg^{2+} mentioned above and Na^{+} *vs* H^{+} [29]). In addition, the incorporation of M^{2+} ions in monoclinic titanates is shown to induce substantial lattice deformation and collapse of layered structure, even resulting in permanent entrapment of the ions within lattice [34]. Furthermore, we examined the ion release of 2QID immersed in PS for 60 days again in PS (Fig. S3, SI), showing that the 60 days immersed 2QID can still release the doped ions, exhibiting the total release amount of the co-doped ions comparable to or higher than M^{2+}-doped $Na_xH_{2-x}Ti_yO_{2y+1}$ and $Na_2Ti_yO_{2y+1}$ [20,26,30–32].

The bond strengths of the coatings were characterized by the scratch-tested critical loads along with their evolution with immersion in PS (Fig. 2e), showing that the incorporation of multi-ions improves, in increased sequence, the bond strengths of primitive DID, 1QID and 2QID coatings compared to ST coating. This might be owing to that the incorporation of multi-ions into nanogranulates adjacent to Ti (EDX spectrum in Fig. 1d) enlarges local interplanar distance, which likely generates residual compressive stress at nanogranulates/Ti interface and thus strengthens the interface (Fig. 2f (left); Fig. S4 (left), SI). After immersion in PS for 60 days, the co-doped coatings exhibit a slight decline in bond strength but less than 10%, and delaminate at the nanorod/granulate interfaces at critical loads (Fig. 2f (right); Fig. S4 (right), SI), displaying a good long-term stability of bond strength. Regarding to surface feature, ST and the multi-ions doped nanrods coated Ti reveal a roughness and hydrophilicity identical to each other without the effect of ion doping, but higher than bare Ti (Fig. S5, SI).

3.2. *Macrophage responses to the ions co-doped nanorods-arrayed coatings*

MΦ responses to DID, 1QID and 2QID coated Ti were assayed along with planar Ti and nanorod-like ST coated Ti as controls by incubating MΦs on the discs for 6–168 h. The ions co-doped nanorod-like arrays, in particular 2QID, promote MΦs to adhere (denoted by more vinculin-marked focal adhesions), spread (mirrored by well-organized actin) and transit in cell shape from rotundity to spindle compared to ST and more significantly to Ti (Fig. S6, SI). This shape shift of MΦs on ST *vs* Ti corresponds to the change in CCR-7 (M1 marker) and Arg-1 (M2 marker) expression, at mRNA and protein levels, of MΦs on ST and Ti over time (Fig. 3a and b), as proven to be contributed to topography-derived M1-to-M2 shift in our previous work [17]. For the ions co-doped arrays, which have identical topography to the control ST (Fig. 1a *vs.* 1d), they show a higher ability of M1 polarization at 6 h, especially 2QID stimulates MΦs to express the highest level of CCR-7 mRNA and the lowest level of Arg-1 mRNA among the arrays; since 24 h, they evoke MΦs to reciprocally express CCR-7 and Arg-1 (Fig. 3a and b) favoring M2 state.

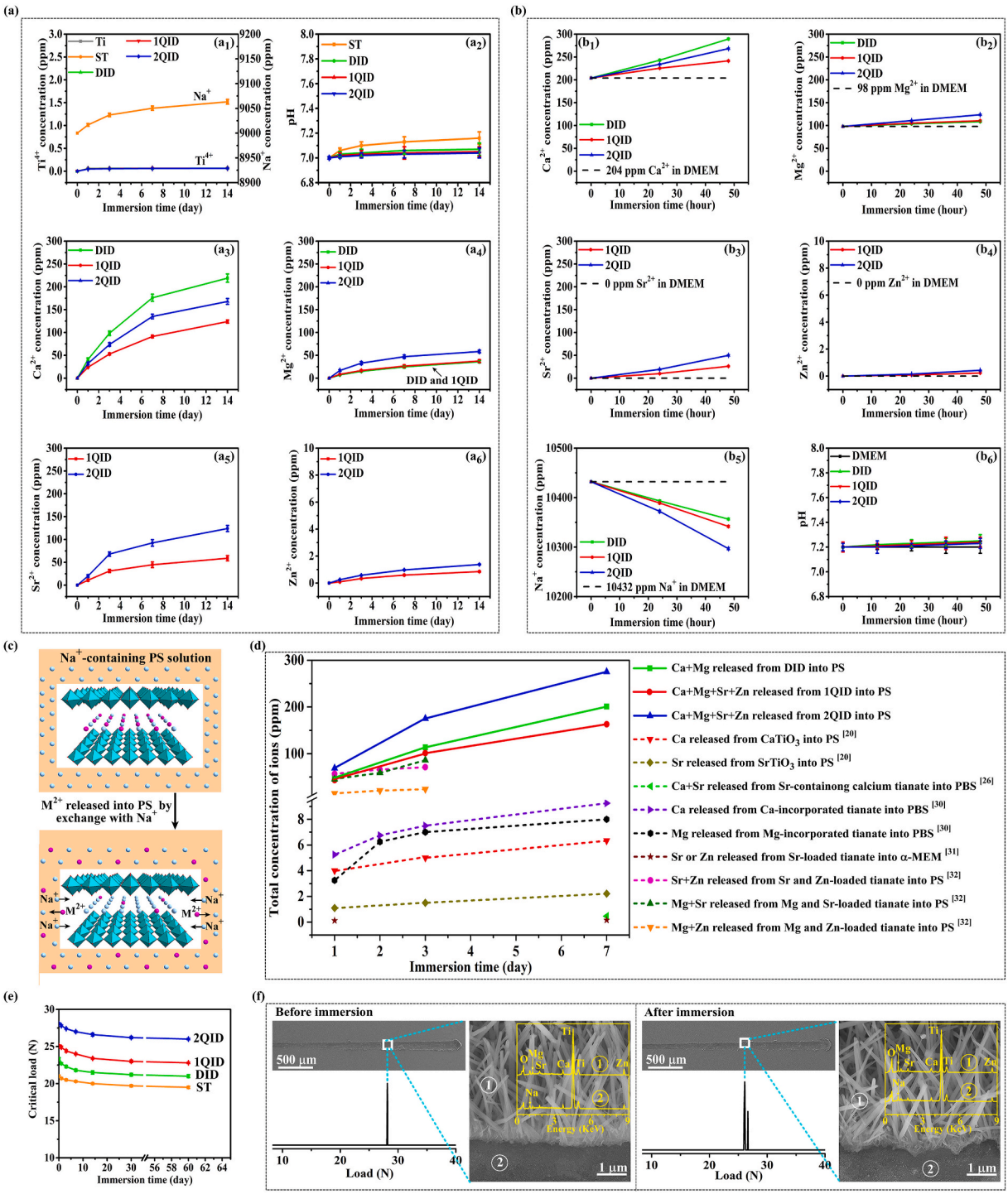

Fig. 2. (a) Ti^{4+}, Ca^{2+}, Mg^{2+}, Sr^{2+} and Zn^{2+} concentrations and pH values of the PS solutions immersing ST, DID, 1QID and 2QID coatings and bare Ti disc as a function of immersion time, along with Na^{+} concentration of PS solution immersing ST; no precipitation appearing during immersion. (b) Ca^{2+}, Mg^{2+}, Sr^{2+}, Zn^{2+} and Na^{+} concentrations and pH values of DMEM immersing ST, DID, 1QID and 2QID coatings as a function of immersion time; no precipitation appearing during immersion. (c) Schematic diagram of M^{2+} (= Ca^{2+}, Mg^{2+}, Sr^{2+} and/or Zn^{2+}) release from our M^{2+} co-doped titaniates with layered structure into PS or DMEM via exchange with Na^{+}. (d) Total concentration of Ca^{2+}, Mg^{2+}, Sr^{2+} and/or Zn^{2+} ions released from our coatings and literature-reported ions-doped titanates [20,26, 30–32], normalized in 1 mL media as a function of immersion time. (e) Bond strengths characterized by the scratch-tested critical loads of the coatings in PS over immersion time, and (f) representative scratch evaluation of 2QID coating before and after 60 days of immersion in PS solution: curve of acoustic output versus load, scratch panoramic morphology, amplified image of initially delaminating area, and EDX spectra detected on the ①-marked nanorods and ②-marked delaminating region.

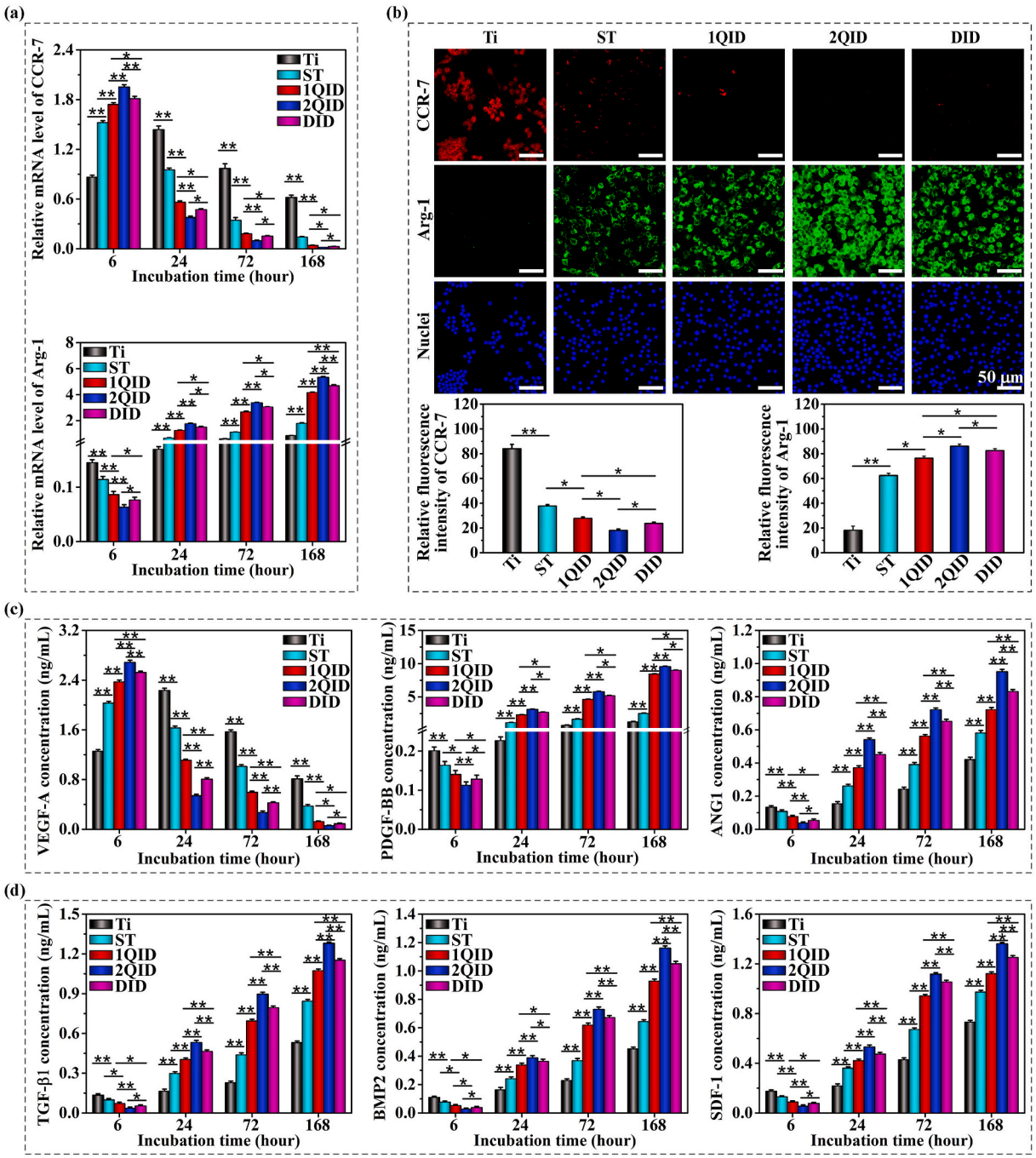

Fig. 3. Response of the seeded MΦs to ST, 1QID, 2QID and DID coated Ti along with bare Ti as a control. (a) mRNA expressions of CCR-7 (M1 marker) and Arg-1 (M2 marker) at 6, 24, 72 and 168 h of incubation. (b) CCR-7 (red), Arg-1 (green) and nuclei (blue) fluorescence staining images and relative contents at protein level of CCR-7 and Arg-1 at 72 h. Secretion of (c) angiogenic cytokines (VEGF-A, PDGF-BB and ANG1), and (d) osteogenic cytokines (TGF-β1, BMP2 and SDF-1) by macrophages at 6, 24, 72 and 168 h *$p < 0.05$, **$p < 0.01$. (For interpretation of the references to colour in this figure legend, the reader is referred to the Web version of this article.)

It is indicated that 2QID has an ability of M1 polarization at 6 h and M2 shift since 24 h higher than DID and much higher than 1QID. Accordingly, compared to ST, at 6 h the ions co-doped arrays elicit MΦs to significantly upregulate the secretion of angiogenic factor — VEGF-A, but prominently downregulate the secretion of angiogenic factors — PDGF-BB and ANG1 (Fig. 3c), and osteogenic factors — TGF-β1, BMP2 and SDF-1 (Fig. 3d). Since 24 h, the co-doped arrays greatly downregulate the secretion of VEGF-A (Fig. 3c), and pro-inflammatory cytokines TNF-α and IL-1β (Fig. S7a, SI); but prominently upregulate the secretion of angiogenic PDGF-BB and ANG1 (Fig. 3c), osteogenic TGF-β1, BMP2 and SDF-1 (Fig. 3d) as well as anti-inflammatory cytokines IL-4 and IL-10 (Fig. S7b, SI). Relatively, 2QID reveals a regulatory ability of MΦs to secrete the mediators higher than DID and much higher than 1QID. The aforementioned up/down-regulation, derived by the co-doped arrays, are more pronounced compared to Ti. Of note, the above-mentioned MΦs-secreted mediators are roughly classified based on initially found function. Taken together, our co-doped arrays, specifically 2QID, can elicit MΦs in a M1 response at 6 h and in a M2 response since 24 h to timely achieve M1-to-M2 shift via releasing ions compared to ST. They also incur the phenotype-dependent secretion of

diverse mediators from MΦs over time, which is consistent with the findings that M1 cells secrete high levels of VEGF-A, TNF-α and IL-1β, while M2 cells produce high levels of TGF-β1, BMP2, PDGF-BB, IL-4 and IL-10 [41–45], but also SDF-1 [46,47] and ANG1 [48,49].

As a main pro-inflammatory transcription factor in diverse cells, nuclear factor κB (NFκB, comprising p65 and p50) is sequestered in cytoplasm in unstimulated cells due to association with its inhibitor IκB [50,51]. MΦs recognize the foreign bodies via binding molecular ligands such as bacterial lipopolysaccharide (LPS) [52–54] and materials-adsorbed proteins [55–57] to cell membrane located Toll-like receptors (TLRs). The ligand-TLR4 binding fosters assembly of Myddosome (containing MyD88 and kinase IRAK, etc.) and subsequently activates IκB kinase (IKK) to phosphorylate IκB and NFκB (*p*-NFκB), leading to IκB degradation, translocation of *p*-NFκB into nucleus, transcription of pro-inflammatory genes and M1 response [52–57]. In parallel, TLR4 activation by ligands such as LPS, elicits Ca^{2+} influx to MΦs via the store-operated Ca^{2+} channel (SOCC) and the chanzyme TRPM7, leading to rise of intracellular Ca^{2+} concentration ($[Ca^{2+}]_i$) [52–54].

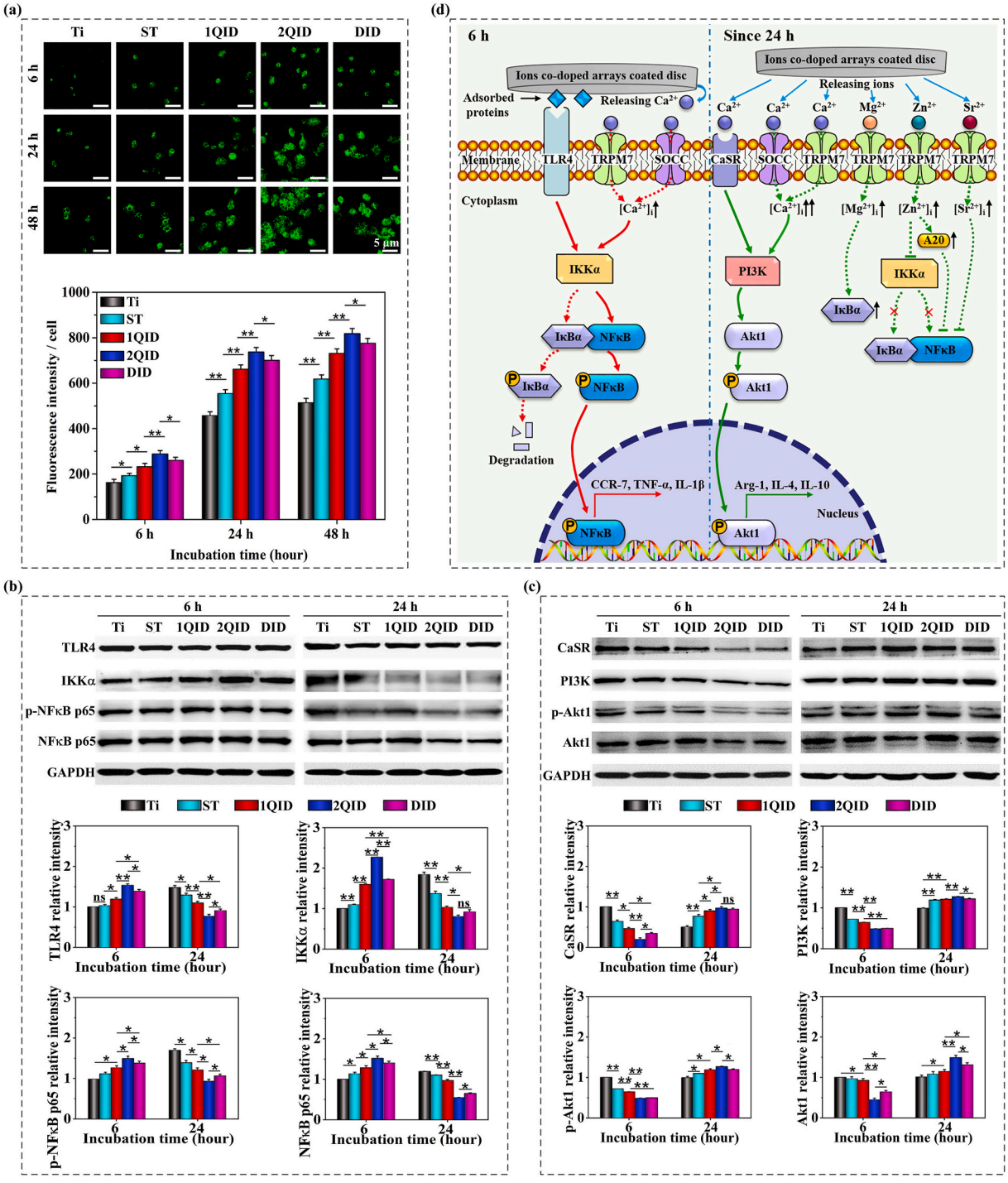

Fig. 4. (a) Flour-4 AM staining images of intracellular Ca^{2+} in MΦs cultured on Ti, ST, 1QID, 2QID and DID at 6, 24 and 48 h along with quantification of fluorescence intensities. Representative western blots and the corresponding quantification of (b)TLR4, IKKα, *p*-NFκB p65 and NFκB p65 as well as (c) CaSR, PI3K, *p*-Akt1 and Akt1 of MΦs cultured on the samples for 6 and 24 h, normalized with GAPDH. (d) Schematic illustration of the molecular mechanism by which the arrays-released ions act on macrophage polarization. *$p < 0.05$, **$p < 0.01$, and ns: no significant.

The $[Ca^{2+}]_i$ rise activates calmodulin-dependent protein kinase II (CaMKII) which activates IKK, promoting nuclear translocation of NFκB [58]. In this context, infrared light-manipulated $[Ca^{2+}]_i$ rise reportedly promotes M1 polarization and vice versa promotes M2 polarization [59]. Similarly, the Ca^{2+} decrease in DMEM media of MΦs, conditioned separately by β-$Ca_3(PO_4)_2$, $MgSiO_3$ and $Sr_2MgSi_2O_7$ due to CaP deposition on the ceramics, was reported to contribute in major part to M2 shift [60–62]. Collectively, these reports support that TLR4 activation and/or $[Ca^{2+}]_i$ rise induce MΦs towards a M1 phenotype. On the other side, CaSR is known to express in many cells including MΦs, and responds to agonists such as di/tri-valent cations and polypeptides [63–65]. Reportedly, elevated extracellular Ca^{2+} concentration ($[Ca^{2+}]_e$), such as 3–14 mM (*vs* 1.8 mM in DMEM), enhances CaSR synthesis and activates CaSR [66–69]. CaSR activation inhibits NFκB activity [68], also stimulates PI3K and its effector kinase Akt [67]. In parallel, CaSR activation by an agonist such as poly-L-lysine, is given to incur $[Ca^{2+}]_i$ rise owing to Ca^{2+} influx through SOCC and release from the Ca^{2+} store [69]. Increased $[Ca^{2+}]_i$ (Fig. 4a) upregulates the activity of PI3K (Fig. 4c), which further phosphorylates and thus activates Akt1 in MΦs [70,71]. Given that PI3K-Akt1 signalling prefers to M2 polarization of MΦs [50,51], thus CaSR activation and/or $[Ca^{2+}]_i$ rise induce MΦs towards a M2 phenotype.

The above phenotypic response of MΦs to Ca^{2+} seems to be reportedly controversial: M1 phenotype [60–62] contrary to M2 phenotype [14,21,33] in response to materials supplied Ca^{2+}, and M1 phenotype [52,59,72] contrary to M2 phenotype [69] in response to $[Ca^{2+}]_i$ rise. To clarify this query and why our ions co-doped arrays elicit MΦs in a M1 response at 6 h and alternatively in a M2 response since 24 h, we examined $[Ca^{2+}]_i$, TLR4 and its downstream molecules (IKKα and NFκB) as well as CaSR and its effector molecules (PI3K and Akt1) of MΦs on the arrays coated and bare Ti discs. At each time of 6, 24 and 48 h, MΦs on the discs exhibit $[Ca^{2+}]_i$ in the order of 2QID > DID > 1QID > ST > Ti (Fig. 4a). Notably, the arrays, particularly 2QID and DID, trigger MΦs to show far more elevated $[Ca^{2+}]_i$ since 24 h (in M2 response) than at 6 h (in M1 response), speculatively exceeding a hypothetic threshold value of $[Ca^{2+}]_i$ that is likely to exist but has not yet been determined, possibly responsible for priming of an alternative signalling pathway; however, the $[Ca^{2+}]_i$ of MΦs on Ti at 24 h is speculatively not in excess of the hypothetic threshold value based on the sustained M1 phenotype at 6 and 24 h. As shown in Fig. 4b drawn by Western blot, TLR4, IKKα and *p*-NFκB p65 protein expressions of MΦs on the discs reveals a variation in the order of 2QID > DID > 1QID > ST ≥ Ti at 6 h, but the inverted order at 24 h. It is indicated that TLR4-NFκB signalling is enhanced in MΦs on the co-doped arrays (especially 2QID) compared to Ti and acts dominantly at 6 h, and nor does it at 24 h when this signalling still predominately acts on the Ti-seeded MΦs. This likely ascribes to the elevated but still at relatively low level of $[Ca^{2+}]_i$ in MΦs seeded on the co-doped arrays at 6 h, as given that IKK activity and nuclear translocation of NFκB are Ca^{2+}-sensitive [50,51,58]. On the other branch, CaSR, PI3K and phosphorylated Akt1 (*p*-Akt1) protein expressions of MΦs on the discs reveals a change in the order of 2QID < or ≈ DID < 1QID < ST < Ti at 6 h, but the inverted order of 2QID > Ti at 24 h (Fig. 4c), indicating that CaSR-PI3K-Akt1 signalling is enhanced in MΦs on the co-doped arrays (especially 2QID) compared to Ti and acts predominately since 24 h. This ascribes to the more elevated $[Ca^{2+}]_i$ that likely exceeds a threshold in MΦs on the co-doped arrays since 24 h. Our data (Fig. 4a–c) also suggest that the rise in both $[Ca^{2+}]_e$ and $[Ca^{2+}]_i$ can induce either M1 or M2 polarization, depending on the magnitude of $[Ca^{2+}]_i$ rise; once the elevated $[Ca^{2+}]_i$ exceeds a threshold, MΦs are stimulated in M2 response, otherwise in M1 response. This finding seems able to coordinate the reported controversial recognitions on phenotypic response to $[Ca^{2+}]$.

Besides Ca^{2+}, the co-doped arrays released other ions also contribute to M2 polarization. Reportedly, extracellular addition of Mg^{2+} elevates its intracellular content ($[Mg^{2+}]_i$) and IκB level, leading to the reduced activation of NFκB and production of inflammatory cytokines [73,74]. Extracellularly adding Sr^{2+} inhibits M1 response, acting as inhibition of NFκB activation [57]. Imported Zn^{2+} inhibits NFκB activation via inactivating IKK and up-regulating the expression of the zinc-finger protein A20 that is NFκB inhibitory [75,76]. Although we did not examine the according ion channels, TRPM7 has been identified to contribute to the entry of Ca^{2+} [53], Mg^{2+} [74], Sr^{2+} and Zn^{2+} [77–79], and the elevation of their intracellular contents. Collectively, our ions co-doped arrays, in particular 2QID, modulate DMEM culture media of MΦs to elevate the extracellular concentrations of Ca^{2+}, Mg^{2+}, Sr^{2+} and/or Zn^{2+} slightly at 6 h but more pronouncedly since 24 h (Fig. 2b) and so does $[Ca^{2+}]_i$ (Fig. 4a); slightly increased $[Ca^{2+}]$ enhances TLR4-NFκB signalling at 6 h (Fig. 4b) while more elevated $[Ca^{2+}]$ enhances CaSR-PI3K-Akt1 signalling (Fig. 4c) and in parallel the considerable rise of intracellular Mg^{2+}, Sr^{2+} and Zn^{2+} inhibits NFκB activation since 24 h, leading to the time-dependent M1/M2 response. Taken together, the underlying mechanism by which the arrays-released ions act on M1 polarization at 6 h and M2 polarization since 24 h is schematically shown in Fig. 4d.

3.3. Angiogenic response of endothelial cells to the coatings-released ions/-conditioned macrophages in vitro

HIF1α, expressed by all extant metazoan species, acts as a transcription factor to regulate downstream genes, encoding multiple angiogenic factors such as VEGF, PDGF-BB, ANG1 and SDF-1 [80]. Individual ions are proven to affect EC response. Apart from hypoxia [80], extracellular ions Ca^{2+}, Sr^{2+} and Mg^{2+} are each shown to markedly stimulate HIF1α expression, while Zn^{2+} shows weakly effect on HIF1α in ECs [81–83]. Moreover, Mg^{2+}, Zn^{2+} and Sr^{2+} individually promote EC migration and the expression of angiogenic genes in ECs, but Ca^{2+} exhibits adverse effects [84,85]. However, the synergistic effect of the quadruple ions on EC angiogenic response remains clarified. To this end, we conducted assays of human umbilical vein ECs (HUVECs) in response to DID, 1QID and 2QID released ions (Fig. S8, SI) and conditioned MΦs together with the released ions (Fig. 5), respectively. In both cases of transwell mono-culture (Fig. S8a in SI) and co-culture (Fig. 5a), compared to ST and Ti, the co-doped arrays promote the migration of HUVECs across TPM to recruit onto TPM bottom side (Fig. S8b, SI; Fig. 5b). They enhance the mRNA expressions of HIF-1α, VEGF-A and PDGF-BB, the secretion of VEGF-A, PDGF-BB and BMP2 (Fig. S8c, d in SI; Fig. 5c and d), and the protein expression of intracellular HIF-1α (Fig. S9a in SI) by the recruited HUVECs. They also incur the enhanced tubular assemble of the recruited HUVECs (Fig. S8e, SI; Fig. 5e). Clearly, these enhanced profiles by the co-doped arrays follow the order of 2QID > DID > 1QID, attributing solely to ionic action on HUVECs and corresponding to the total release amounts of multi-ions (Fig. 2d) in transwell culture case, while ascribing to the actions of both the released ions and the conditioned MΦs-secreted factors on HUVECs in the case of transwell co-culture.

As depicted in Fig. 3 and S7 (SI), the ions co-doped arrays, especially 2QID, regulate MΦs to favor M1 state at 6 h and M2 state since 24 h compared to ST: the M1 secrete high levels of VEGF-A, TNF-α and IL-1β, while the M2 cells produce high levels of PDGF-BB, ANG1, TGF-β1, BMP2, SDF-1, IL-4 and IL-10. Reportedly, the transcription factor HIF-1α can be induced by growth factors TGF-β1 and PDGF-BB as well as cytokines in normoxia [86], and TNF-α and IL-4 enhance HIF-1α mRNA and protein levels [87–90]. The high levels of such mediators secreted by MΦs on our ions-doped arrays (Fig. 3c and d; Fig. S7, SI), thereby, contribute to the enhanced HIF-1α expression at mRNA and protein levels in HUVECs co-cultured with the conditioned MΦs (Fig. 5c; Fig. S9a, SI), which encodes VEGF-A and PDGF-BB [80] and enhances their syntheses in HUVECs (Fig. 5c and d). Previous works have verified the roles of cells-secreted factors in regulating the behavior and tubule formation of endothelial progenitor cells (EPCs) and ECs. VEGF-A, PDGF-BB, TGF-β1 and SDF-1 are each shown to promote migration and tubule formation of EPCs to different extent [91,92], among which

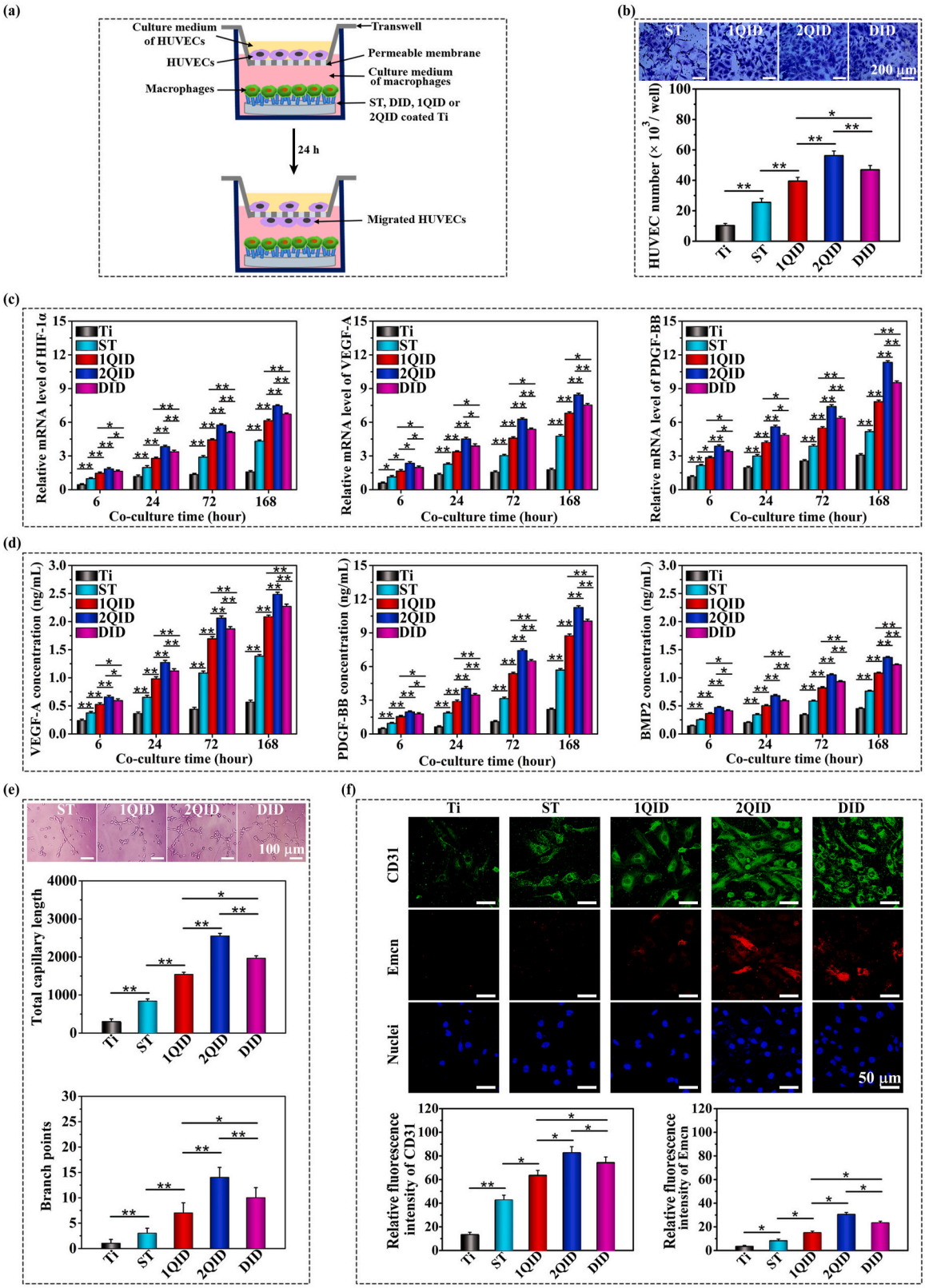

Fig. 5. Response of HUVECs seeded on TPM to MΦs seeded on ST, 1QID, 2QID and DID coated discs along with bare Ti. (a) Schematic diagram for co-culture of HUVECs and MΦs. (b) Crystal violet staining images and counting of the HUVECs migrated across TPM at 24 h. (c) mRNA expressions of HIF-1α, VEGF-A and PDGF-BB, and (d) secretion of VEGF-A, PDGF-BB and BMP2 by the HUVECs recruited onto TPM bottom side. (e) Images of the recruited HUVECs constructed capillaries at 6 h as well as counting of total capillary length and branch point per imaged field. (f) Fluorescence staining images and relative intensities of CD31 (green) and Emcn (red) performed on the migrated HUVECs at 72 h *$p < 0.05$, **$p < 0.01$. (For interpretation of the references to colour in this figure legend, the reader is referred to the Web version of this article.)

SDF-1 and VEGF-A have the strongest promotion respectively on EPC migration and tubule formation [92]. Regarding ECs, VEGF-A and ANG1 are each given to stimulate migration towards a factor gradient, and to promote tubule networking of ECs [93,94]. PDGF-BB and SDF-1 strongly stimulate EC migration [92,95], while TGF-β1 and BMP2 promote tube formation [7]. Like VEGF-A, pro-inflammatory TNF-α and IL-1β are each shown to stimulate ECs to recruit and to prime ECs for sprouting [41]. Intriguingly, VEGF-A can also trigger ECs to produce osteogenic factor BMP2 [9]. Owing to the factor secretion profiles of our arrays conditioned MΦs, the aforementioned enhancement of HUVEC behaviors and tubule assemble, derived by the ions co-doped arrays relative to ST and Ti, is more pronounced in response to both the ionic action and the MΦs-secreted factors (Fig. 5b–e) than in sole response to ionic action on HUVECs (Fig. S8b-e and S9a, SI). These results also suggest that M1 cells are important initiators of angiogenesis, and M2 MΦs are also necessary for angiogenesis.

Intriguingly, DID and in particular 2QID are shown to render highly expressed positive CD31 and Emcn in the recruited HUVECs co-cultured

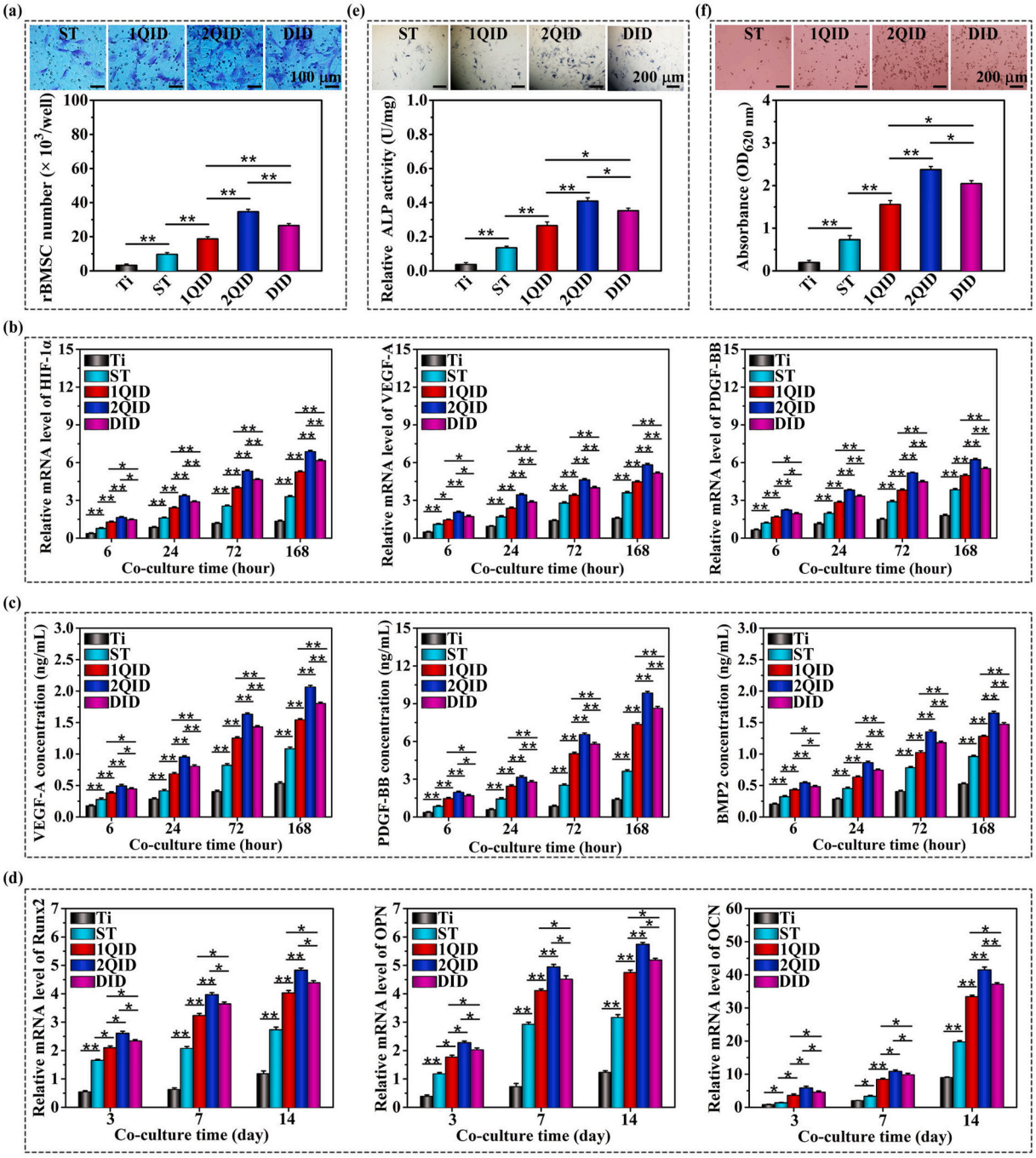

Fig. 6. Response of rBMSCs seeded on TPM to MΦs seeded on ST, 1QID, 2QID and DID coated discs along with bare Ti (likewise co-cultured schematically as HUVECs in Fig. 5a). (a) Crystal violet staining images and counting of the rBMSCs migrated across TPM at 24 h. (b) mRNA expressions of HIF-1α, VEGF-A and PDGF-BB, (c) secretion of VEGF-A, PDGF-BB and BMP2, and (d) mRNA expressions of Runx2, OPN and OCN by the rBMSCs recruited onto TPM bottom side. (e) Staining images and activity quantification of ALP produced by the recruited rBMSCs at 3 d. (f) Alizarin Red staining images of extracellular matrix produced by the recruited rBMSCs and quantification of mineralized nodules at 14 d *$p < 0.05$, **$p < 0.01$. (For interpretation of the references to colour in this figure legend, the reader is referred to the Web version of this article.)

with MΦs (Fig. 5f), suggesting that these HUVECs-assembled tubules are type-H classified owing to the $CD31^{hi}Emcn^{hi}$ feature [12]. While DID and in particular 2QID trigger MΦs to secrete much higher level of PDGF-BB than 1QID, ST and Ti (in descending order) since 24 h, consequently contributing in most part to assembling of type-H tubules, as given that PDGF-BB induces formation of type-H capillaries during bone modeling and remodeling [91].

3.4. Osteogenic response of MSCs to the coatings-released ions/-conditioned MΦs in vitro

Like ECs [96–99], MSCs, as one kind of osteogenesis-related cells, are also able to secrete angiogenic factors VEGF [9,10], PDGF-BB [95], ANG1 and SDF-1 [99]. Individual ions are given to affect MSC response. Besides Co^{2+} and Cu^{2+} [100,101], Mg^{2+} also elicits HIF1α expression in MSCs [102]. Sr^{2+} enhances the synthesis of VEGF and ANG1 in MSCs [94]. Moreover, Ca^{2+}, Mg^{2+}, Zn^{2+} and Sr^{2+} are each shown to promote the migration [103–105] and osteo-differentiation [27,30–33,94] of MSCs. However, the collaborative action of the multi-ions on MSC migration and angio/osteo-genic response remains elusive, especially in the presence of MΦs. To this end, we assessed the responses of rat bone marrow-derived MSCs (rBMSCs) to DID, 1QID and 2QID released ions (Fig. S10, SI) and to the arrays conditioned MΦs and released ions (Fig. 6), via transwell culture and co-culture ways (schematically as Fig. S8a and 5a with rBMSCs instead of HUVECs), respectively. In both cases of the mono/co-culture manners, compared to ST and Ti, the co-doped arrays markedly stimulate migration of rBMSCs to recruit onto TPM bottom side (Fig. S10a, SI; Fig. 6a). They trigger the recruited rBMSCs to highly express angiogenic HIF-1α, VEGF-A and PDGF-BB mRNAs (Fig. S10b, SI; Fig. 6b), HIF-1α protein (Fig. S9b in SI), and to secrete VEGF-A, PDGF-BB and BMP2 pronouncedly (Fig. S10c, SI; Fig. 6c). Simultaneously, they render the recruited rBMSCs to differentiate and mineralize ECM markedly, as evidenced by the fortified mRNA expressions of osteogenic factors Runx2, OPN and OCN (Fig. S10d, SI; Fig. 6d), ALP activities (Fig. S10e, SI; Fig. 6e), and mineralization of calcium nodules (Fig. S10f, SI; Fig. 6f). Clearly, these enhanced profiles, derived by the ions co-doped arrays, follow the order of 2QID > DID > 1QID, attributing solely to ionic action on rBMSCs in transwell culture case and in line with the total release amounts of the doped multi-ions, while ascribing to the actions of both the released ions and MΦs-secreted factors on rBMSCs in co-culture case. Notably, these enhanced responses of rBMSCs are more pronounced to the synergistic actions (Fig. 6a–f) than to the sole action of the released ions (Fig. S10a-f and S9b, SI) for each of 2QID, DID and 1QID.

Previous works have clarified the roles of cells-secreted factors in regulating the migration and angio/osteo-genic response of MSCs. VEGF-A, PDGF-BB, TGF-β1 and SDF-1 are each shown to foster MSC migration more or less [91,92], among which SDF-1 shows the strongest promotion on MSC migration *in vitro* [92] and significant recruiting action on MSCs *ex vivo* [46,47]. Regarding angiogenic response, TGF-β1, PDGF-BB, IL-1β, TNF-α and IL-4 are exemplified to increase HIF-1α expression in normoxia [86–90], and HIF-1α encodes VEGF-A and PDGF-BB [80]. On osteogenic response, TGF-β1 and in particular BMP2 are well known to induce osteo-differentiation of MSCs [7,9]. Intriguingly, VEGF-A can stimulate MSCs and osteoblasts to synthesize and secrete BMP2 [9,10], and likewise ANG1 also enhances osteoblast differentiation via concomitantly potentiated BMP2 signalling [7]. Alternatively, PDGF-BB increase osteo-differentiation of MSCs via the extracellular signal-related kinase 1/2 signalling [95]. Pro-inflammatory IL-1β and TNF-α suppress but anti-inflammatory IL-4 and IL-10 enhance osteoblastic differentiation and ECM mineralization [5]. Based on these findings, in combination of the profiles of the factors secreted by MΦs conditioned with our arrays, it is reasonably supported that the enhanced migration, expression and secretion of angiogenic factors, osteo-differentiation and ECM mineralization of rBMSCs, derived by the ions co-doped arrays relative to ST, are more pronounced in transwell co-culture case than in transwell mono-culture case. It is also suggested that the M1 MΦs are initiators while the M2 MΦs are necessary for osteogenesis, and the most important is timely M1-to-M2 turnover.

3.5. In vivo cellular response, histological identification and bone-implant integration of the arrays-coated screws

We implanted ST, DID, 1QID and 2QID coated and bare Ti screws into femoral condyles of Sprague-Dawley rats for a series of periods to assess cellular response, histological evolution and osseointegration. By immunofluorescence staining of the thin sections that the screws were removed, the images used for identifying the cells adjacent to the screws-removed spaces (SRS) were obtained, representatively as Fig. 7a, panoramically showing the stained CCR-7/Arg-1 for MΦs, CD31/Emcn for ECs, and CD90 (a specific marker of MSCs [46]) besides stained nuclei. The magnified images show that the cells surrounding screws become more with implantation time (Fig. 7b). 1QID, DID and in particular 2QID peripherally show CCR-7 highly positive ($CCR\text{-}7^{+}$) M1 cells sparsely but Arg-1 highly positive ($Arg\text{-}1^{+}$) M2 cells more at days 1 and 3, contrary to ST and Ti (Fig. 7c). CD31-marked ECs are more around the ions co-doped arrays than ST and Ti at day 1, and become more pronounced around each kind of the co-doped arrays with implantation to 3 days (Fig. 7d), indicating a strong role of the co-doped arrays in EC recruitment. Notably, the ECs around DID and in particular 2QID present highly positive CD31 and Emcn at day 3 (Fig. 7d), implying the enhanced $CD31^{hi}Emcn^{hi}$ subset of ECs and thus formation of type-H capillaries [12] around both the arrays. In addition, CD90-marked MSCs are visible around DID and especially 2QID but almost invisible around 1QID, ST and Ti at day 1 (Fig. 7e). However, MSCs are less in amount than ECs and much less than MΦs around 2QID and DID at day 1, indicating earlier recruitment of ECs than MSCs; this likely ascribes to high levels of the secreted VEGF-A, TNF-α and IL-1β by early polarized M1 MΦs (Fig. 3; Fig. S7a, SI), which are each given to powerfully stimulate EC recruitment [41,93,94]. Moreover, MSCs become more pronounced around each kind of the arrays with implantation from day 1 to day 3, suggesting a strong role of the arrays in MSC recruitment; however, MSCs become less with further implantation to day 7 (Fig. 7e and f). Concomitantly, highly positive Col-1 and OPN appear markedly around 1QID, DID and specifically 2QID compared to ST and Ti at days 3 and 7, and become more pronounced with implantation from days 3 to 7 for each of the ions co-doped arrays (Fig. 7e and f). It is indicated that 1QID, DID and especially 2QID stimulate osteoblastic differentiation of the surrounding MSCs to secret ECM components (e.g., Col-1, OPN, etc.), and thereby resulting in the decrease in amount of MSCs at day 7. Collectively, the ions co-doped arrays (in particular 2QID) enhance the recruitment and $CD31^{hi}Emcn^{hi}$ subset of ECs as well as the recruitment and osteo-differentiation of MSCs in endosseous milieu.

HE and Masson staining of the screws-removed thin sections were also conducted to identify inflammatory reaction and bone forming ability. HE staining shows that at week 2 of implantation, a few of inflammatory cells still infiltrate into sparse collagen marked osteoid matrix around Ti; however, the osteoid matrices around the arrays tend to be compact in the order of ST, 1QID, DID and 2QID, without infiltration of inflammatory cells (Fig. 8a). At week 4, the osteoid matrices around 1QID, DID and especially 2QID become mature (given by deepened red), with osteocytes embedding within and osteoblasts arranging at the periphery of osteoid matrices (Fig. 8a). Masson staining of the osteoid matrices around the arrays and Ti shows a similar trend to HE staining. Notably, capillaries (red arrows) are pronounced around the ions co-doped arrays (in particular 2QID) at weeks 2 and 4, while the surrounding osteoid matrices become mature (as deepened blue) and increase in quantity with prolonging implantation to 4 weeks (Fig. 8b), indicating the formation of vascularized bone.

In vivo, ECs assemble the tubular network of mural cells-uncovered

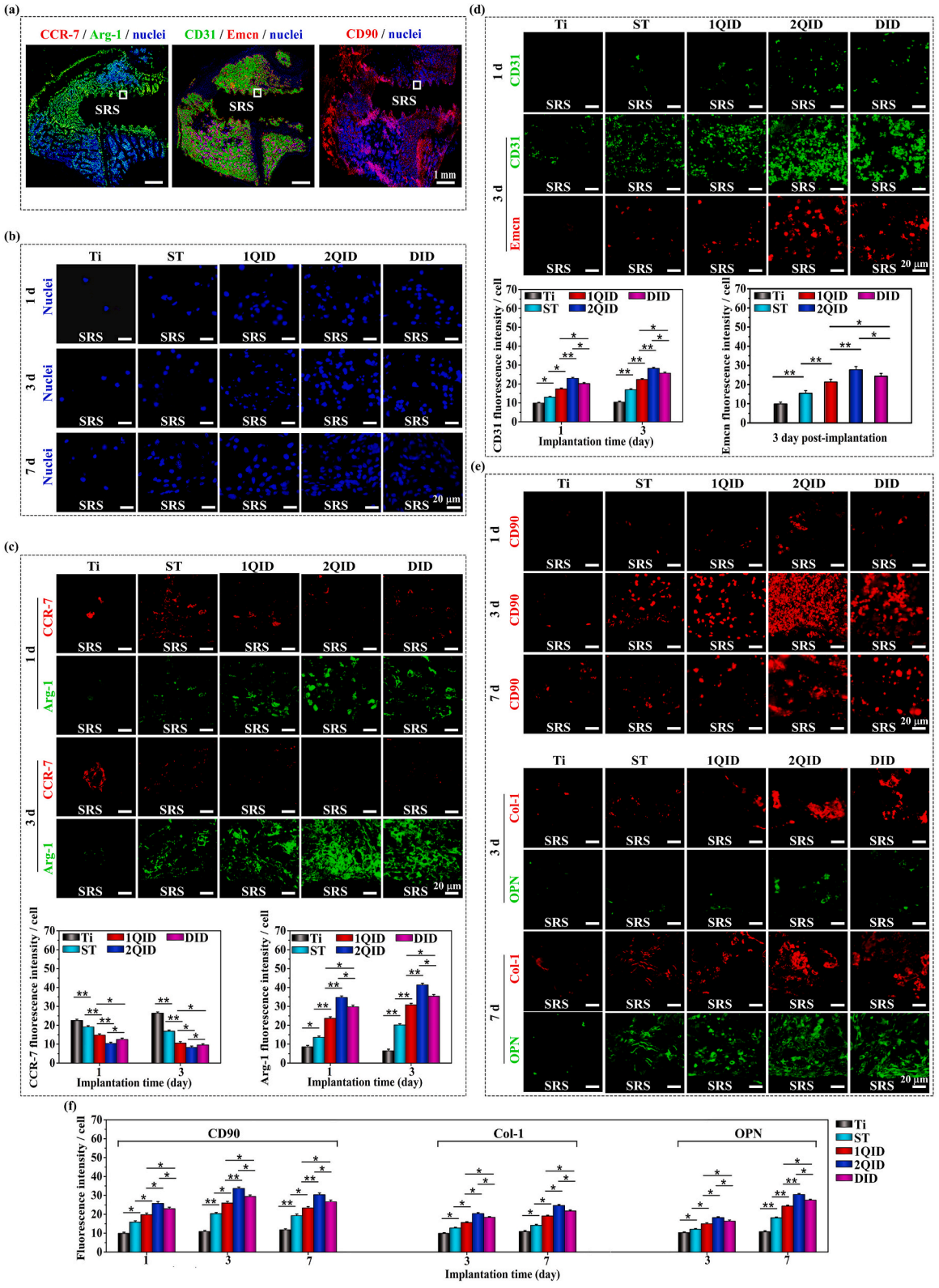

Fig. 7. Fluorescent staining analyses of MΦs, ECs, MSCs and MSC osteo-differentiation within the tissues surrounding the spaces remained after removing the coated and bare Ti screws implanted in rat femoral condyles for 1, 3 and 7 d. (a) Examples for panoramic images of CCR-7/Arg-1/nuclei, CD31/Emcn/nuclei and CD90/nuclei adjacent to the screws-removed spaces (SRS). Following magnified fluorescent staining images were taken from white rectangle-marked regions adjacent to SRS as schematically shown in (a). (b) Magnified images of cell nuclei (blue) at 1, 3 and 7 d. (c) Magnified images of CCR-7 (red) and Arg-1 (green), along with CCR-7 or Arg-1 fluorescence intensity per cell at 1 and 3 d. (d) Magnified images of CD31 (green) at 1 d as well as CD31 (green) and Emcn (red) at 3 d, together with CD31 and Emcn fluorescence intensity per cell. (e) Magnified images of CD90 (red) at 1, 3 and 7 d as well as Col-1 (red) and OPN (green) at 3 and 7 d. (f) Fluorescence intensity per cell of CD90, Col-1 and OPN. *$p < 0.05$, **$p < 0.01$. (For interpretation of the references to colour in this figure legend, the reader is referred to the Web version of this article.)

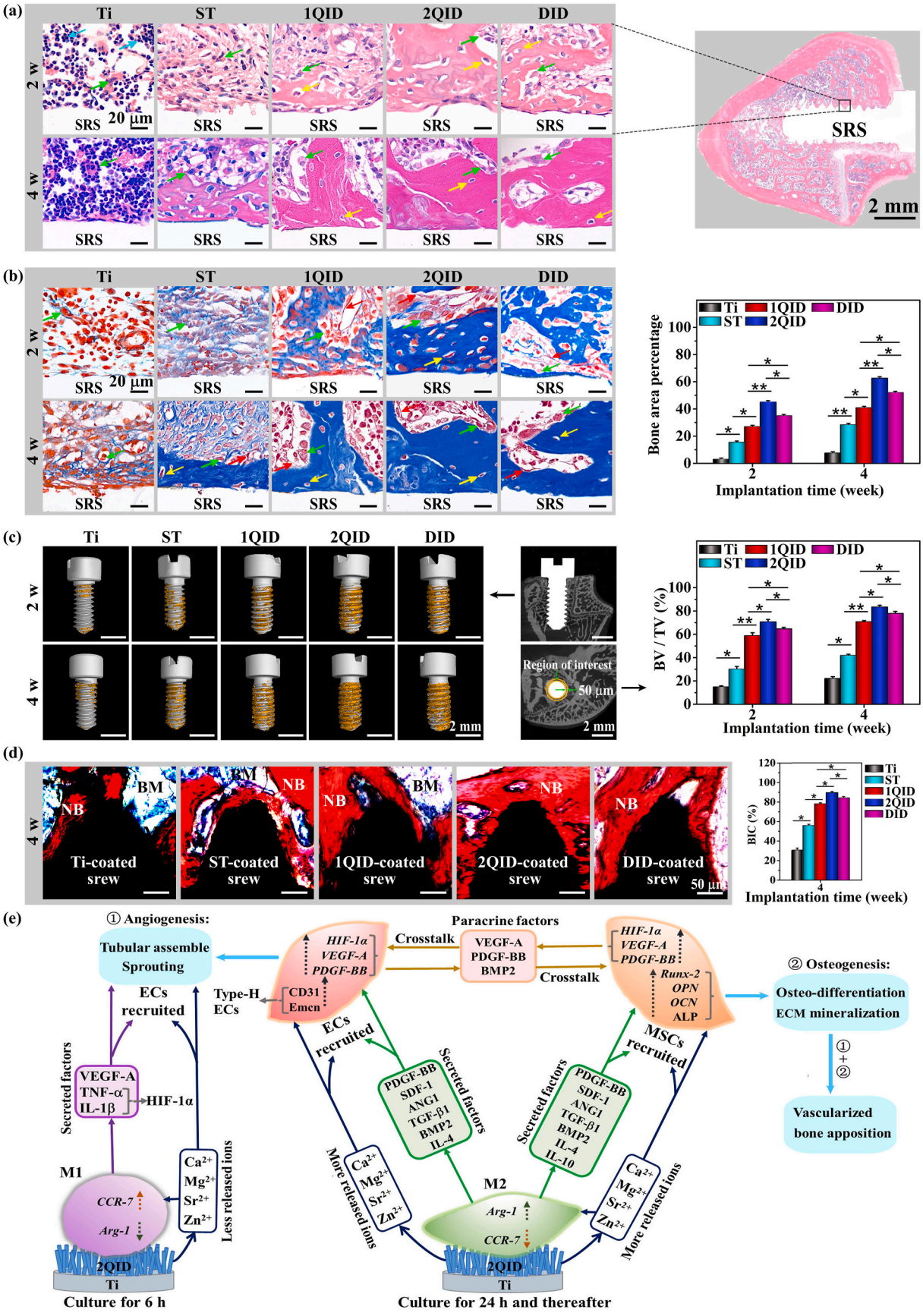

(caption on next page)

Fig. 8. HE and Masson staining analyses of the tissues surrounding the spaces remained after removing the coated and bare Ti screws implanted in rat femoral condyles for 2 and 4 weeks; green arrows indicating osteoblasts, yellow arrows representing osteocytes embedded in bone matrix, cyan arrows indicating inflammatory cells, red arrows indicating blood vessels. (a) An example of HE staining panoramic architecture (right), and magnified images of the regions adjacent to the screws-removed spaces (SRS); red stained zone indicating nascent bone, dark pink zones indicating osteoid tissue. (b) Masson staining magnified images of the regions adjacent to SRS (blue stained zone indicating nascent bone, and dark blue zones indicating osteoid tissue), and percentage of bone area to total area. Micro-CT and VG staining characterized formation of new bone surrounding the screws implanted in rat femoral condyles. (c) (middle) Micro-CT laterally and vertically viewed images of the condyle containing screws, (left) reconstructed images of the newly formed bone around screws and (right) bone volume/total volume (BV/TV) in the region of interest with a width of 50 μm from the screw (marked in vertically viewed image) at 2 and 4 weeks. (d) VG staining images of bone surrounding the screws at 4 weeks (BM: bone marrow, NB: new bone), and corresponding bone-implant contact ratios (BIC). *$p < 0.05$, **$p < 0.01$. (e) Schematically showing immunomodulatory outline for regulating angiogenesis and osteogenesis by our muli-ions co-doped arrays. (For interpretation of the references to colour in this figure legend, the reader is referred to the Web version of this article.)

endothelium. Blood vessel formation by angiogenesis includes multi-steps: new capillary sprouting, sprout growth, anastomosis, and maturation by recruiting pericytes to cover endothelium [96–98]. VEGF-A is a principal initiator of capillary sprouting and the most crucial molecule controlling vascular morphogenesis [96]. In response to VEGF-A, some ECs within capillary wall are organized as tip-cells for sprouting, trailed by stalk-cells that retain connectivity with parental vessels. Sprout outgrowth continues toward VEGF-A gradient until neighboring tip-cells connect and fuse with each other (i.e., anastomosis) under the aid of MΦs [97,98]. To function properly, capillaries must be mature. Several factors PDGF-BB, TGF-β1, ANG1 and SDF-1 contribute to maturation by chemoattracting pericytes to cover ECs [97,98], while the binding of ANG1 to its receptor TIE2 promotes pericyte association to endothelium [96]. Our co-doped arrays (especially 2QID) regulate MΦs to early secrete high levels of VEGF-A, TNF-α and IL-1β (each given to initiate sprouting of ECs [41]) then to secrete high levels of PDGF-BB, TGF-β1, ANG1 and SDF-1 acting on vascular maturation, and thereby are expected to benefit to the formation of mature vessels.

Micro-CT reconstructed 3D images (Fig. 8c) show that new bone forms sparsely around Ti screw, pronouncedly around ST-coated screw, and more pronouncedly around 1QID, DID and especially 2QID coated screws at 2 and 4 weeks post implantation into rat femoral condyles. This is also supported by the quantitation of the bone volume/total volume (BV/TV) within the ring region of 50 μm in width around an implanted screw. VG staining images (Fig. 8d) show that at week 4 of implantation, the new bone around the arrays coated and bare Ti screws presents the same trend in quantity as depicted by micro-CT. Notably, the new bone apposition actions quantified by the bone-to-implant contact (BIC) ratios of the screws are rather different. The BIC ratio tends to increase in the order of Ti, ST, 1QID, DID and 2QID, even reaches ~85% for 2QID-coated screw, indicating a super osseointegration of 2QID.

Collectively, DID reveals the response profiles of MΦs, HUVECs and rBMSCs as well as the abilities of angiogenesis, osteogenesis and osseointegration higher than 1QID but lower than 2QID. Correspondingly, DID has a Mg^{2+} doping dose and total doping dose of multi-ions similar to 1QID and a Ca^{2+} doping dose ~2.7 times of that in 1QID, while 2QID has a doping dose of individual ions about twice of that in 1QID. It is indicated that in the case of equivalent total doping dose of multi-ions, the elevated Ca^{2+} doping dose is beneficial to the improvement of biological properties (based on DID *vs* 1QID). On the other hand, in the case of relatively higher Ca^{2+} doping dose, the co-incorporation of additional Mg^{2+}, Sr^{2+} and Zn^{2+} sounds to more significantly improve the biological properties of the co-doped ST derivants (based on 2QID *vs* DID). This also confirms the beneficial role of the primary Ca^{2+} and trace Mg^{2+}, Sr^{2+} and Zn^{2+} contained within bone mineral in bone modeling and remodeling [37].

Taken together, our results identify that the ions co-doped arrays (representatively 2QID), via releasing ions, polarize MΦs to favor M1 cells at 6 h and M2 cells since 1 day, and M1 cells secrete high levels of VEGF-A, TNF-α and IL-1β while M2 cells secrete high levels of PDGF-BB, ANG1, TGF-β1, BMP2, SDF-1, IL-4 and IL-10 *in vitro* (Fig. 3; Fig. S7, SI). *In vivo*, 2QID array also stimulates the peripheral MΦs to greatly favor Arg-1^+ M2 cells since 1 day (Fig. 7c). With the actions of the released ions and conditioned MΦs-secreted factors, 2QID promotes the recruitment of ECs and MSCs (Figs. 5b and 6a) but more early for ECs than MSCs (Fig. 7d and e). Also, 2QID promotes the secretion of VEGF-A, PDGF-BB and BMP2 by the recruited ECs (Fig. 5d) and MSCs (Fig. 6c), tubular assemble (Fig. 5e) and formation of type-H capillaries (Figs. 5f and 7d), MSC osteo-differentiation and ECM mineralization (Fig. 6d–f, 7e). These enhanced cellular responses by 2QID consequently promote the formation and apposition of vascularized bone on its surface (Fig. 8a–d). Overall, the immunomodulation of angiogenesis and osteogenesis, derived by our ions co-doped arrays (representatively 2QID), is schematically demonstrated in Fig. 8e. In this schema, besides the MΦs mediated immunomodulation of ECs and MSCs, both kinds of the cells are also considered to interplay *in vivo* via the paracrine factors VEGF-A, PDGF-BB and BMP2. This is exemplified by that VEGF-A can positively regulate the synthesis and secretion of BMP2 in ECs, MSCs and osteoblasts [9,10], while BMP2 can trigger osteoblasts to produce VEGF-A [10], and by that PDGF-BB induces type-H vessels, mobilizing cells of mesenchymal origin and orchestrating cellular components for osteoblastic differentiation [91].

4. Conclusion

Dual (Ca^{2+} and Mg^{2+}) and quadruple (Ca^{2+}, Mg^{2+}, Sr^{2+} and Zn^{2+}) ions co-doped Na_2TiO_3 nanorods arrayed coatings have been hydrothermally grown on Ti. The co-doped ions partially substitute Na^+ in Na_2TiO_3 and are able to efficiently release out from cubic lattice via exchange with Na^+ in fluid rather than dissolution, endowing the coatings superior long-term stability of structure and bond strength. The co-doped coatings, particularly 2QID, elevate the extracellular concentrations of the ions and MΦ intracellular [Ca^{2+}] to different extent with time. Regulated by the ion profiles, TLR4-NFκB signalling is enhanced and acts primarily at early stage while CaSR-PI3K-Akt1 signalling is then enhanced and acts predominately in MΦs, triggering MΦs in a M1 response at 6 h and in a M2 response since 24 h to secrete diverse cytokines. With the actions of the released ions and secreted cytokines, the co-doped coatings (in particular 2QID) promotes the recruitment of ECs and MSCs, tubular assemble and type-H capillary formation, MSC osteo-differentiation and ECM mineralization, and apposition of vascularized bone.

Data availability

The raw data and methods in this work are available upon request.

CRediT authorship contribution statement

Dongmei Yu: Methodology, Investigation, Software, Formal analysis, Visualization, Data curation, Validation. **Bo Li:** Methodology, Investigation, Software, Formal analysis, Visualization, Data curation, Validation. **Meng Yu:** Methodology, Investigation, Software, Formal analysis, Visualization, Data curation, Validation. **Shuo Guo:** Partial cell and animal tests, Visualization. **Zheng Guo:** Resources, Supervision. **Yong Han:** Conceptualization, Writing – original draft, Writing – review & editing, Funding acquisition, Supervision.

Declaration of competing interest

The authors declare that they have no known competing financial interests or personal relationships that could have appeared to influence the work reported in this paper.

Acknowledgment

The authors greatly appreciate the financial support from the National Natural Science Foundation of China (Grant number 51631007 and 51971171).

Appendix A. Supplementary data

Supplementary data to this article can be found online at https://doi.org/10.1016/j.bioactmat.2022.01.039.

References

[1] L.M. Sun, C.C. Berndt, K.A. Gross, A. Kucuk, Material fundamentals and clinical performance of plasma-sprayed hydroxyapatite coatings: a review, J. Biomed. Mater. Res. 58 (2001) 570–592, https://doi.org/10.1002/jbm.1056.
[2] R.A. Surmenev, M.A. Surmeneva, A.A. Ivanova, Significance of calcium phosphate coatings for the enhancement of new bone osteogenesis - a review, Acta Biomater. 10 (2014) 557–579, https://doi.org/10.1016/j.actbio.2013.10.036.
[3] J.E. Davies, Bone bonding at natural and biomaterial surfaces, Biomaterials 28 (2007) 5058–5067, https://doi.org/10.1016/j.biomaterials.2007.07.049.
[4] M.O. Dellacherie, B.R. Seo, D.J. Mooney, Macroscale biomaterials strategies for local immunomodulation, Nat. Rev. Mater. 4 (2019) 379–397, https://doi.org/10.1038/s41578-019-0106-3.
[5] J. Lee, H. Byun, S.K.M. Perikamana, S. Lee, H. Shin, Current advances in immunomodulatory biomaterials for bone regeneration, Adv. Healthc. Mater. 8 (2019) 1801106, https://doi.org/10.1002/adhm.201801106.
[6] D. Hachim, S.T. LoPresti, C.C. Yates, B.N. Brown, Shifts in macrophage phenotype at the biomaterial interface via IL-4 eluting coatings are associated with improved implant integration, Biomaterials 112 (2017) 95–107, https://doi.org/10.1016/j.biomaterials.2016.10.019.
[7] L. Bai, Z. Du, J. Du, W. Yao, J. Zhang, Z. Weng, S. Liu, Y. Zhao, Y. Liu, X. Zhang, X. Huang, X. Yao, R. Crawford, R. Hang, D. Huang, B. Tang, Y. Xiao, A multifaceted coating on titanium dictates osteoimmunomodulation and osteo/angio-genesis towards ameliorative osseointegration, Biomaterials 162 (2018) 154–169, https://doi.org/10.1016/j.biomaterials.2018.02.010.
[8] P.C. Qiu, M.B. Li, K. Chen, B. Fang, P.F. Chen, Z.B. Tang, X.F. Lin, S.W. Fan, Periosteal matrix-derived hydrogel promotes bone repair through an early immune regulation coupled with enhanced angio- and osteogenesis, Biomaterials 227 (2020) 119552, https://doi.org/10.1016/j.biomaterials.2019.119552.
[9] S. Stegen, N. van Gastel, G. Carmeliet, Bringing new life to damaged bone: the importance of angiogenesis in bone repair and regeneration, Bone 70 (2015) 19–27, https://doi.org/10.1016/j.bone.2014.09.017.
[10] A. Grosso, M.G. Burger, A. Lunger, D.J. Schaefer, A. Banfi, N. Di Maggio, It takes two to tango: coupling of angiogenesis and osteogenesis for bone regeneration, Front. Bioeng. Biotechnol. 5 (2017) 68, https://doi.org/10.3389/fbioe.2017.00068.
[11] U.H. Langen, M.E. Pitulescu, J.M. Kim, R. Enriquez-Gasca, K.K. Sivaraj, A. P. Kusumbe, A. Singh, J. Di Russo, M.G. Bixel, B. Zhou, L. Sorokin, J. M. Vaquerizas, R.H. Adams, Cell-matrix signals specify bone endothelial cells during developmental osteogenesis, Nat. Cell Biol. 19 (2017) 189–201, https://doi.org/10.1038/ncb3476.
[12] A.P. Kusumbe, S.K. Ramasamy, R.H. Adams, Coupling of angiogenesis and osteogenesis by a specific vessel subtype in bone, Nature 507 (2014) 323–328, https://doi.org/10.1038/nature13145.
[13] W.J. Zhang, G.C. Wang, Y. Liu, X.B. Zhao, D.H. Zou, C. Zhu, Y.Q. Jin, Q.F. Huang, J. Sun, X.Y. Liu, X.Q. Jiang, H. Zreiqat, The synergistic effect of hierarchical micro/nano-topography and bioactive ions for enhanced osseointegration, Biomaterials 34 (2013) 3184–3195, https://doi.org/10.1016/j.biomaterials.2013.01.008.
[14] Y. Huang, C.T. Wu, X.L. Zhang, J. Chang, K.R. Dai, Regulation of immune response by bioactive ions released from silicate bioceramics for bone regeneration, Acta Biomater. 66 (2018) 81–92, https://doi.org/10.1016/j.actbio.2017.08.044.
[15] E. Goyenvalle, E. Aguado, J.M. Nguyen, N. Passuti, L. Le Guehennec, P. Layrolle, G. Daculsi, Osteointegration of femoral stem prostheses with a bilayered calcium phosphate coating, Biomaterials 27 (2006) 1119–1128, https://doi.org/10.1016/j.biomaterials.2005.07.039.
[16] J.H.C. Yang, K. Teii, C.C. Chang, S. Matsumoto, M. Rafailovich, Biocompatible cubic boron nitride: a noncytotoxic ultrahard material, Adv. Funct. Mater. 31 (2021) 2005066, https://doi.org/10.1002/adfm.202005066.
[17] H.W. Yang, M. Yu, R. Wang, B. Li, X. Zhao, Y.L. Hao, Z. Guo, Y. Han, Hydrothermally grown TiO_2-nanorods on surface mechanical attrition treated Ti: improved corrosion fatigue and osteogenesis, Acta Biomater. 116 (2020) 400–414, https://doi.org/10.1016/j.actbio.2020.09.005.
[18] W. Dong, T. Zhang, J. Epstein, L. Cooney, H. Wang, Y. Li, Y.B. Jiang, A. Cogbill, V. Varadan, Z.R. Tian, Multifunctional nanowire bioscaffolds on titanium, Chem. Mater. 19 (2007) 4454–4459, https://doi.org/10.1021/cm070845a.
[19] Y.C. Xin, J. Jiang, K.F. Huo, T. Hu, P.K. Chu, Bioactive $SrTiO_3$ nanotube arrays: strontium delivery platform on Ti-based osteoporotic bone implants, ACS Nano 3 (2009) 3228–3234, https://doi.org/10.1021/nn9007675.
[20] H.S. Kim, Y.J. Kim, J.H. Jang, J.W. Park, Surface engineering of nanostructured titanium implants with bioactive ions, J. Dent. Res. 95 (2016) 558–565, https://doi.org/10.1177/0022034516638026.
[21] C.H. Lee, Y.J. Kim, J.H. Jang, J.W. Park, Modulating macrophage polarization with divalent cations in nanostructured titanium implant surfaces, Nanotechnology 27 (2016), https://doi.org/10.1088/0957-4484/27/8/085101, 085101.
[22] Y. Li, X.P. Gao, G.R. Li, G.L. Pan, T.Y. Yan, H.Y. Zhu, Titanate nanofiber reactivity: fabrication of $MTiO_3$ (M = Ca, Sr, and Ba) perovskite oxides, J. Phys. Chem. C 113 (2009) 4386–4394, https://doi.org/10.1021/jp810805f.
[23] W.J. Dong, B.J. Li, Y. Li, X.B. Wang, L.N. An, C.R. Li, B.Y. Chen, G. Wang, Z. Shi, General approach to well-defined perovskite $MTiO_3$ (M = Ba, Sr, Ca, and Mg) nanostructures, J. Phys. Chem. C 115 (2011) 3918–3925, https://doi.org/10.1021/jp110660v.
[24] J. Coreno, O. Coreno, Evaluation of calcium titanate as apatite growth promoter, J. Biomed. Mater. Res. A 75A (2005) 478–484, https://doi.org/10.1002/jbm.a.30447.
[25] T. Kizuki, H. Takadama, T. Matsushita, T. Nakamura, T. Kokubo, Preparation of bioactive Ti metal surface enriched with calcium ions by chemical treatment, Acta Biomater. 6 (2010) 2836–2842, https://doi.org/10.1016/j.actbio.2010.01.007.
[26] S. Yamaguchi, S. Nath, T. Matsushita, T. Kokubo, Controlled release of strontium ions from a bioactive Ti metal with a Ca-enriched surface layer, Acta Biomater. 10 (2014) 2282–2289, https://doi.org/10.1016/j.actbio.2014.01.026.
[27] Y. Okuzu, S. Fujibayashi, S. Yamaguchi, K. Yamamoto, T. Shimizu, T. Sono, K. Goto, B. Otsuki, T. Matsushita, T. Kokubo, S. Matsuda, Strontium and magnesium ions released from bioactive titanium metal promote early bone bonding in a rabbit implant model, Acta Biomater. 63 (2017) 383–392, https://doi.org/10.1016/j.actbio.2017.09.019.
[28] S. Spriano, S. Yamaguchi, F. Baino, S. Ferraris, A critical review of multifunctional titanium surfaces: new frontiers for improving osseointegration and host response, avoiding bacteria contamination, Acta Biomater. 79 (2018) 1–22, https://doi.org/10.1016/j.actbio.2018.08.013.
[29] S. Ferraris, S. Yamaguchi, N. Barbani, M. Cazzola, C. Cristallini, M. Miola, E. Verne, S. Spriano, Bioactive materials: in vitro investigation of different mechanisms of hydroxyapatite precipitation, Acta Biomater. 102 (2020) 468–480, https://doi.org/10.1016/j.actbio.2019.11.024.
[30] N. Ren, J.H. Li, J.C. Qiu, Y.H. Sang, H.D. Jiang, R.I. Boughton, L. Huang, W. Huang, H. Liu, Nanostructured titanate with different metal ions on the surface of metallic titanium: a facile approach for regulation of rBMSCs fate on titanium implants, Small 10 (2014) 3169–3180, https://doi.org/10.1002/smll.201303391.
[31] G.S. Wang, Y. Wan, B. Ren, T. Wang, Z.Q. Liu, Surface functionalization of micro/nanostructured titanium with bioactive ions to regulate the behaviors of murine osteoblasts, Adv. Eng. Mater. 19 (2017) 1700299, https://doi.org/10.1002/adem.201700299.
[32] X.X. Song, W. Tang, D. Gregurec, L. Yate, S.E. Moya, G.C. Wang, Layered titanates with fibrous nanotopographic features as reservoir for bioactive ions to enhance osteogenesis, Appl. Surf. Sci. 436 (2018) 653–661, https://doi.org/10.1016/j.apsusc.2017.12.027.
[33] J.X. Gong, M. Sun, S.L. Wang, J.X. He, Y. Wang, Y. Qian, Y. Liu, L.Q. Dong, L. Ma, K. Cheng, W.J. Weng, M.F. Yu, Y.S. Zhang, H.M. Wang, Surface modification by divalent main-group-elemental ions for improved bone remodeling to instruct implant biofabrication, ACS Biomater. Sci. Eng. 5 (2019) 3311–3324, https://doi.org/10.1021/acsbiomaterials.9b00270.
[34] N. Li, L.D. Zhang, Y.Z. Chen, M. Fang, J.X. Zhang, H.M. Wang, Highly efficient, irreversible and selective ion exchange property of layered titanate nanostructures, Adv. Funct. Mater. 22 (2012) 835–841, https://doi.org/10.1002/adfm.201102272.
[35] W. Liu, J.H. Li, M.Q. Cheng, Q.J. Wang, K.W.K. Yeung, P.K. Chu, X.L. Zhang, Zinc-modified sulfonated polyetheretherketone surface with immunomodulatory function for guiding cell fate and bone regeneration, Adv. Sci. 5 (2018) 1800749, https://doi.org/10.1002/advs.201800749.
[36] X.W. Yuan, H.L. Cao, J.X. Wang, K.W. Tang, B. Li, Y.C. Zhao, M.Q. Cheng, H. Qin, X.Y. Liu, X.L. Zhang, Immunomodulatory effects of calcium and strontium Co-doped titanium oxides on osteogenesis, Front. Immunol. 8 (2017) 1196, https://doi.org/10.3389/fimmu.2017.01196.
[37] V. Zaichick, S. Zaichick, V. Karandashev, S. Nosenko, The effect of age and gender on Al, B, Ba, Ca, Cu, Fe, K, Li, Mg, Mn, Na, P, S, Sr, V, and Zn contents in rib bone of healthy humans, Biol. Trace Elem. Res. 129 (2009) 107–115, https://doi.org/10.1007/s12011-008-8302-9.
[38] Y.V. Kolen'ko, K.A. Kovnir, A.I. Gavrilov, A.V. Garshev, J. Frantti, O.I. Lebedev, B.R. Churagulov, G. Van Tendeloo, M. Yoshimura, Hydrothermal synthesis and characterization of nanorods of various titanates and titanium dioxide, J. Phys. Chem. B 110 (2006) 4030–4038, https://doi.org/10.1021/jp055687u.
[39] M. Nouri-Felekori, M. Khakbiz, N. Nezafati, Synthesis and characterization of Mg, Zn and Sr-incorporated hydroxyapatite whiskers by hydrothermal method, Mater. Lett. 243 (2019) 120–124, https://doi.org/10.1016/j.matlet.2019.01.147.

[40] D.H. Kim, S.G. Oh, C.G. Cho, Effects of Cs and Na ions on the interfacial properties of dodecyl sulfate solutions, Colloid Polym. Sci. 279 (2001) 39–45, https://doi.org/10.1007/s003960000393.
[41] K.L. Spiller, R.R. Anfang, K.J. Spiller, J. Ng, K.R. Nakazawa, J.W. Daulton, G. Vunjak-Noyakovic, The role of macrophage phenotype in vascularization of tissue engineering scaffolds, Biomaterials 35 (2014) 4477–4488, https://doi.org/10.1016/j.biomaterials.2014.02.012.
[42] K.L. Spiller, S. Nassiri, C.E. Witherel, R.R. Anfang, J. Ng, K.R. Nakazawa, T. Yu, G. Vunjak-Novakovic, Sequential delivery of immunomodulatory cytokines to facilitate the M1-to-M2 transition of macrophages and enhance vascularization of bone scaffolds, Biomaterials 37 (2015) 194–207, https://doi.org/10.1016/j.biomaterials.2014.10.017.
[43] S.A. Eming, T.A. Wynn, P. Martin, Inflammation and metabolism in tissue repair and regeneration, Science 356 (2017) 1026–1030, https://doi.org/10.1126/science.aam7928.
[44] S. Adams, L.M. Wuescher, R. Worth, E. Yildirim-Ayan, Mechano-immunomodulation: mechanoresponsive changes in macrophage activity and polarization, Ann. Biomed. Eng. 47 (2019) 2213–2231, https://doi.org/10.1007/s10439-019-02302-4.
[45] C.E. Witherel, D. Abebayehu, T.H. Barker, K.L. Spiller, Macrophage and fibroblast interactions in biomaterial-mediated fibrosis, Adv. Healthc. Mater. 8 (2019) 1801451, https://doi.org/10.1002/adhm.201801451.
[46] Q. Zhang, J.W. Hwang, J.H. Oh, C.H. Park, S.H. Chung, Y.S. Lee, J.H. Baek, H. M. Ryoo, K.M. Woo, Effects of the fibrous topography-mediated macrophage phenotype transition on the recruitment of mesenchymal stem cells: an in vivo study, Biomaterials 149 (2017) 77–87, https://doi.org/10.1016/j.biomaterials.2017.10.007.
[47] J.E. Won, Y.S. Lee, J.H. Park, J.H. Lee, Y.S. Shin, C.H. Kim, J.C. Knowles, H. W. Kim, Hierarchical microchanneled scaffolds modulate multiple tissue-regenerative processes of immune-responses, angiogenesis, and stem cell homing, Biomaterials 227 (2020) 119548, https://doi.org/10.1016/j.biomaterials.2019.119548.
[48] H.P. Gu, M. Cui, Y. Bai, F.R. Chen, K.T. Ma, C.Y. Zhou, L.J. Guo, Angiopoietin-1/Tie2 signaling pathway inhibits lipopolysaccharide-induced activation of RAW264.7 macrophage cells, Biochem. Bioph. Res. Co. 392 (2010) 178–182, https://doi.org/10.1016/j.bbrc.2010.01.009.
[49] T. Li, H.S. Ma, H.Z. Ma, Z.J. Ma, L. Qiang, Z.Z. Yang, X.X. Yang, X.J. Zhou, K. R. Dai, J.W. Wang, Mussel-inspired nanostructures potentiate the immunomodulatory properties and angiogenesis of mesenchymal stem cells, ACS Appl. Mater. Interfaces 11 (2019) 17134–17146, https://doi.org/10.1021/acsami.8b22017.
[50] T. Lawrence, G. Natoli, Transcriptional regulation of macrophage polarization: enabling diversity with identity, Nat. Rev. Immunol. 11 (2011) 750–761, https://doi.org/10.1038/nri3088.
[51] D.X. Zhou, C. Huang, Z. Lin, S.X. Zhan, L.N. Kong, C.B. Fang, J. Li, Macrophage polarization and function with emphasis on the evolving roles of coordinated regulation of cellular signaling pathways, Cell. Signal. 26 (2014) 192–197, https://doi.org/10.1016/j.cellsig.2013.11.004.
[52] Y.X. Ye, X.Y. Huang, Y.X. Zhang, X.Q. Lai, X.P. Wu, X.F. Zeng, X.G. Tang, Y. Y. Zeng, Calcium influx blocked by SK&F 96365 modulates the LPS plus IFN-gamma-induced inflammatory response in murine peritoneal macrophages, Int. Immunopharm. 12 (2012) 384–393, https://doi.org/10.1016/j.intimp.2011.12.011.
[53] S.M.S. Schappe, K. Szteyn, M.E. Stremska, S.K. Mendu, T.K. Downs, P.V. Seegren, M.A. Mahoney, S. Dixit, J.K. Krupa, E.J. Stipes, J.S. Rogers, S.E. Adamson, N. Leitinger, B.N. Desai, Chanzyme TRPM7 mediates the Ca(2+) influx essential for lipopolysaccharide-induced toll-like receptor 4 endocytosis and macrophage activation, Immunity 48 (2018) 59–74, https://doi.org/10.1016/j.immuni.2017.11.026.
[54] K.A. Fitzgerald, J.C. Kagan, Toll-like receptors and the control of immunity, Cell 180 (2020) 1044–1066, https://doi.org/10.1016/j.cell.2020.02.041.
[55] S. Hao, J. Meng, Y. Zhang, J. Liu, X. Nie, F.X. Wu, Y.L. Yang, C. Wang, N. Gu, H. Y. Xu, Macrophage phenotypic mechanomodulation of enhancing bone regeneration by superparamagnetic scaffold upon magnetization, Biomaterials 140 (2017) 16–25, https://doi.org/10.1016/j.biomaterials.2017.06.013.
[56] A.L. Silva, C. Peres, J. Conniot, A.I. Matos, L. Moura, B. Carreira, V. Sainz, A. Scomparin, R. Satchi-Fainaro, V. Preat, H.F. Florindo, Nanoparticle impact on innate immune cell pattern-recognition receptors and inflammasomes activation, Semin. Immunol. 34 (2017) 3–24, https://doi.org/10.1016/j.smim.2017.09.003.
[57] H. Xing, R. Li, Y.A. Qing, B. Ying, Y. Qin, Biomaterial-based osteoimmunomodulatory strategies via the TLR4-NF-κB signaling pathway: a review, Appl. Mater. Today 22 (2021) 100969, https://doi.org/10.1016/j.apmt.2021.100969.
[58] M.C.X. Pinto, A.H. Kihara, V.A.M. Goulart, F.M.P. Tonelli, K.N. Gomes, H. Ulrich, R.R. Resende, Calcium signaling and cell proliferation, Cell. Signal. 27 (2015) 2139–2149, https://doi.org/10.1016/j.cellsig.2015.08.006.
[59] H. Kang, K.Y. Zhang, D.S.H. Wong, F.X. Han, B. Li, L.M. Bian, Near-infrared light-controlled regulation of intracellular calcium to modulate macrophage polarization, Biomaterials 178 (2018) 681–696, https://doi.org/10.1016/j.biomaterials.2018.03.007.
[60] Z.T. Chen, C.T. Wu, W.Y. Gu, T. Klein, R. Crawford, Y. Xiao, Osteogenic differentiation of bone marrow MSCs by beta-tricalcium phosphate stimulating macrophages via BMP2 signalling pathway, Biomaterials 35 (2014) 1507–1518, https://doi.org/10.1016/j.biomaterials.2013.11.014.
[61] C.T. Wu, Z.T. Chen, D.H. Yi, J. Chang, Y. Xiao, Multidirectional effects of Sr-, Mg-, and Si-containing bioceramic coatings with high bonding strength on inflammation, osteoclastogenesis, and osteogenesis, ACS Appl. Mater. Interfaces 6 (2014) 4264–4276, https://doi.org/10.1021/am4060035.
[62] C.T. Wu, Z.T. Chen, Q.J. Wu, D.L. Yi, T. Friis, X.B. Zheng, J. Chang, X.Q. Jiang, Y. Xiao, Clinoenstatite coatings have high bonding strength, bioactive ion release, and osteoimmunomodulatory effects that enhance in vivo osseointegration, Biomaterials 71 (2015) 35–47, https://doi.org/10.1016/j.biomaterials.2015.08.027.
[63] A.L. Magno, B.K. Ward, T. Ratajczak, The calcium-sensing receptor: a molecular perspective, Endocr. Rev. 32 (2011) 3–30, https://doi.org/10.1210/er.2009-0043.
[64] F.M. Hannan, E. Kallay, W.H. Chang, M.L. Brandi, R.V. Thakker, The calcium-sensing receptor in physiology and in calcitropic and noncalcitropic diseases, Nat. Rev. Endocrinol. 15 (2018) 33–51, https://doi.org/10.1038/s41574-018-0115-0.
[65] K. Leach, F.M. Hannan, T.M. Josephs, A.N. Keller, T.C. Moller, D.T. Ward, E. Kallay, R.S. Mason, R.V. Thakker, D. Riccardi, A.D. Conigrave, H. Brauner-Osborne, International union of basic and clinical pharmacology. CVIII. Calcium-sensing receptor nomenclature, pharmacology, and function, Pharmacol. Rev. 72 (2020) 558–604, https://doi.org/10.1124/pr.119.018531.
[66] Y. Honda, T. Anada, S. Kamakura, M. Nakamura, S. Sugawara, O. Suzuki, Elevated extracellular calcium stimulates secretion of bone morphogenetic protein 2 by a macrophage cell line, Biochem. Bioph. Res. Co. 345 (2006) 1155–1160, https://doi.org/10.1016/j.bbrc.2006.05.013.
[67] D. Peiris, I. Pacheco, C. Spencer, R.J. MacLeod, The extracellular calcium-sensing receptor reciprocally regulates the secretion of BMP-2 and the BMP antagonist Noggin in colonic myofibroblasts, Am. J. Physiol-Gastr. L. 292 (2007) G753–G766, https://doi.org/10.1152/ajpgi.00225.2006.
[68] J.C. Kelly, P. Lungchukiet, R.J. MacLeod, Extracellular calcium-sensing receptor inhibition of intestinal epithelial TNF signaling requires CaSR-mediated Wnt5a/Ror2 interaction, Front. Physiol. 2 (2011) 1–10, https://doi.org/10.3389/fphys.2011.00017.
[69] Y. Mine, H. Zhang, Anti-inflammatory effects of poly-L-lysine in intestinal mucosal system mediated by calcium-sensing receptor activation, J. Agric. Food Chem. 63 (2015) 10437–10447, https://doi.org/10.1021/acs.jafc.5b03812.
[70] J.L. Joyal, D.J. Burks, S. Pons, W.F. Matter, C.J. Vlahos, M.F. White, D.B. Sacks, Communication - calmodulin activates phosphatidylinositol 3-kinase, J. Biol. Chem. 272 (1997) 28183–28186, https://doi.org/10.1074/jbc.272.45.28183.
[71] H.T. Liu, H. Perlman, L.J. Pagliari, R.M. Pope, Constitutively activated Akt-1 is vital for the survival of human monocyte-differentiated macrophages: role of Mcl-1, independent of nuclear factor (NF)-kappa B, bad, or caspase activation, J. Exp. Med. 194 (2001) 113–125, https://doi.org/10.1084/jem.194.2.113.
[72] X. Zhou, W. Yang, J. Li, Ca2+- and protein kinase C-dependent signaling pathway for nuclear factor-kappaB activation, inducible nitric-oxide synthase expression, and tumor necrosis factor-alpha production in lipopolysaccharide-stimulated rat peritoneal macrophages, J. Biol. Chem. 281 (2006) 31337–31347, https://doi.org/10.1074/jbc.M602739200.
[73] J. Sugimoto, A.M. Romani, A.M. Valentin-Torres, A.A. Luciano, C.M.R. Kitchen, N. Funderburg, S. Mesiano, H.B. Bernstein, Magnesium decreases inflammatory cytokine production: a novel innate immunomodulatory mechanism, J. Immunol. 188 (2012) 6338–6346, https://doi.org/10.1016/j.ajog.2011.10.841.
[74] W. Qiao, K.H.M. Wong, J. Shen, W. Wang, J. Wu, J. Li, Z. Lin, Z. Chen, J. P. Matinlinna, Y. Zheng, S. Wu, X. Liu, K.P. Lai, Z. Chen, Y.W. Lam, K.M. C. Cheung, K.W.K. Yeung, TRPM7 kinase-mediated immunomodulation in macrophage plays a central role in magnesium ion-induced bone regeneration, Nat. Commun. 12 (2021) 2885, https://doi.org/10.1038/s41467-021-23005-2.
[75] M.J. Liu, S. Bao, M. Galvez-Peralta, C.J. Pyle, A.C. Rudawsky, R.E. Pavlovicz, D. W. Killilea, C. Li, D.W. Nebert, M.D. Wewers, D.L. Knoell, ZIP8 regulates host defense through zinc-mediated inhibition of NF-kappaB, Cell Rep. 3 (2013) 386–400, https://doi.org/10.1016/j.celrep.2013.01.009.
[76] M. Jarosz, M. Olbert, G. Wyszogrodzka, K. Mlyniec, T. Librowski, Antioxidant and anti-inflammatory effects of zinc. Zinc-dependent NF-kappa B signaling, Inflammopharmacology 25 (2017) 11–24, https://doi.org/10.1007/s10787-017-0309-4.
[77] M.K. Monteilh-Zoller, M.C. Hermosura, M.J.S. Nadler, A.M. Scharenberg, R. Penner, A. Fleig, TRPM7 provides an ion channel mechanism for cellular entry of trace metal ions, J. Gen. Physiol. 121 (2003) 49–60, https://doi.org/10.1085/jgp.20028740.
[78] A. Bouron, K. Kiselyov, J. Oberwinkler, Permeation, regulation and control of expression of TRP channels by trace metal ions, Pflügers Archiv 467 (2015) 1143–1164, https://doi.org/10.1007/s00424-014-1590-3.
[79] S. Zierler, S. Hampe, W. Nadolni, TRPM channels as potential therapeutic targets against pro-inflammatory diseases, Cell Calcium 67 (2017) 105–115, https://doi.org/10.1016/j.ceca.2017.05.002.
[80] G.L. Semenza, Hypoxia-inducible factors in physiology and medicine, Cell 148 (2012) 399–408, https://doi.org/10.1016/j.cell.2012.01.021.
[81] S. Oda, T. Oda, S. Takabuchi, K. Nishi, T. Wakamatsu, T. Tanaka, T. Adachi, K. Fukuda, R. Nohara, K. Hirota, The calcium channel blocker cilnidipine selectively suppresses hypoxia-inducible factor 1 activity in vascular cells, Eur. J. Pharmacol. 606 (2009) 130–136, https://doi.org/10.1016/j.ejphar.2009.01.012.
[82] Y. Yu, G. Jin, Y. Xue, D. Wang, X. Liu, J. Sun, Multifunctions of dual Zn/Mg ion co-implanted titanium on osteogenesis, angiogenesis and bacteria inhibition for dental implants, Acta Biomater. 49 (2017) 590–603, https://doi.org/10.1016/j.actbio.2016.11.067.
[83] J.C. Moses, T. Saha, B.B. Mandal, Chondroprotective and osteogenic effects of silk-based bioinks in developing 3D bioprinted osteochondral interface, Bioprinting 17 (2020), e00067, https://doi.org/10.1016/j.bprint.2019.e00067.

[84] X.J. Guo, S.L. Wei, M.M. Lu, Z.W. Shao, J.Y. Lu, L.G. Xia, K.L. Lin, D.R. Zou, Dose-dependent effects of strontium ranelate on ovariectomy rat bone marrow mesenchymal stem cells and human umbilical vein endothelial cells, Int. J. Biol. Sci. 12 (2016) 1511–1522, https://doi.org/10.7150/ijbs.16499.
[85] H.S. Han, I. Jun, H.K. Seok, K.S. Lee, K. Lee, F. Witte, D. Mantovani, Y.C. Kim, S. Glyn-Jones, J.R. Edwards, Biodegradable magnesium alloys promote angio-osteogenesis to enhance bone repair, Adv. Sci. 7 (2020) 2000800, https://doi.org/10.1002/advs.202000800.
[86] K.G. Pringle, K.L. Kind, A.N. Sferruzzi-Perri, J.G. Thompson, C.T. Roberts, Beyond oxygen: complex regulation and activity of hypoxia inducible factors in pregnancy, Hum. Reprod. Update 16 (2010) 415–431, https://doi.org/10.1093/humupd/dmp046.
[87] M. Scharte, K. Jurk, B. Kehrel, A. Zarbock, H. Van Aken, K. Singbartl, IL-4 enhances hypoxia induced HIF-1alpha protein levels in human transformed intestinal cells, FEBS Lett. 580 (2006) 6399–6404, https://doi.org/10.1016/j.febslet.2006.10.053.
[88] H. Jiang, Y.S. Zhu, H. Xu, Y. Sun, Q.F. Li, Inflammatory stimulation and hypoxia cooperatively activate HIF-1{alpha} in bronchial epithelial cells: involvement of PI3K and NF-{kappa}B, Am. J. Physiol. Lung Cell Mol. Physiol. 298 (2010) L660–L669, https://doi.org/10.1152/ajplung.00394.2009.
[89] S. Tsapournioti, I. Mylonis, A. Hatziefthimiou, M.G. Ioannou, R. Stamatiou, G. K. Koukoulis, G. Simos, P.A. Molyvdas, E. Paraskeva, TNFalpha induces expression of HIF-1alpha mRNA and protein but inhibits hypoxic stimulation of HIF-1 transcriptional activity in airway smooth muscle cells, J. Cell. Physiol. 228 (2013) 1745–1753, https://doi.org/10.1002/jcp.24331.
[90] K.W. Kim, S.J. Lee, J.C. Kim, TNF-alpha upregulates HIF-1alpha expression in pterygium fibroblasts and enhances their susceptibility to VEGF independent of hypoxia, Exp. Eye Res. 164 (2017) 74–81, https://doi.org/10.1016/j.exer.2017.08.008.
[91] H. Xie, Z. Cui, L. Wang, Z.Y. Xia, Y. Hu, L.L. Xian, C.J. Li, L. Xie, J. Crane, M. Wan, G.H. Zhen, Q. Bian, B. Yu, W.Z. Chang, T. Qiu, M. Pickarski, L.T. Duong, J. J. Windle, X.H. Luo, E.Y. Liao, X. Cao, PDGF-BB secreted by preosteoclasts induces angiogenesis during coupling with osteogenesis, Nat. Med. 20 (2014) 1270–1278, https://doi.org/10.1038/nm.3668.
[92] J.L. Sun, K. Jiao, L.N. Niu, Y. Jiao, Q. Song, L.J. Shen, F.R. Tay, J.H. Chen, Intrafibrillar silicified collagen scaffold modulates monocyte to promote cell homing, angiogenesis and bone regeneration, Biomaterials 113 (2017) 203–216, https://doi.org/10.1016/j.biomaterials.2016.10.050.
[93] K. Dashnyam, G.Z. Jin, J.H. Kim, R. Perez, J.H. Jang, H.W. Kim, Promoting angiogenesis with mesoporous microcarriers through a synergistic action of delivered silicon ion and VEGF, Biomaterials 116 (2017) 145–157, https://doi.org/10.1016/j.biomaterials.2016.11.053.
[94] L.X. Mao, L.G. Xia, J. Chang, J.Q. Liu, L.Y. Jiang, C.T. Wu, B. Fang, The synergistic effects of Sr and Si bioactive ions on osteogenesis, osteoclastogenesis and angiogenesis for osteoporotic bone regeneration, Acta Biomater. 61 (2017) 217–232, https://doi.org/10.1016/j.actbio.2017.08.015.
[95] M.L. Zhang, W.W. Yu, K. Niibe, W.J. Zhang, H. Egusa, T.T. Tang, X.Q. Jiang, The effects of platelet-derived growth factor-BB on bone marrow stromal cell-mediated vascularized bone regeneration, Stem Cell. Int. (2018) 3272098, https://doi.org/10.1155/2018/3272098, 2018.
[96] R.H. Adams, K. Alitalo, Molecular regulation of angiogenesis and lymphangiogenesis, Nat. Rev. Mol. Cell Biol. 8 (2007) 464–478, https://doi.org/10.1038/nrm2183.
[97] P. Carmeliet, R.K. Jain, Molecular mechanisms and clinical applications of angiogenesis, Nature 473 (2011) 298–307, https://doi.org/10.1038/nature10144.
[98] S.P. Herbert, D.Y.R. Stainier, Molecular control of endothelial cell behaviour during blood vessel morphogenesis, Nat. Rev. Mol. Cell Biol. 12 (2011) 551–564, https://doi.org/10.1038/nrm3176.
[99] S. Rafii, J.M. Butler, B.S. Ding, Angiocrine functions of organ-specific endothelial cells, Nature 529 (2016) 316–325, https://doi.org/10.1038/nature17040.
[100] W. Fan, R. Crawford, Y. Xiao, Enhancing in vivo vascularized bone formation by cobalt chloride-treated bone marrow stromal cells in a tissue engineered periosteum model, Biomaterials 31 (2010) 3580–3589, https://doi.org/10.1016/j.biomaterials.2010.01.083.
[101] N. Kong, K.L. Lin, H.Y. Li, J. Chang, Synergy effects of copper and silicon ions on stimulation of vascularization by copper-doped calcium silicate, J. Mater. Chem. B 2 (2014) 1100–1110, https://doi.org/10.1039/c3tb21529f.
[102] S. Yoshizawa, A. Brown, A. Barchowsky, C. Sfeir, Magnesium ion stimulation of bone marrow stromal cells enhances osteogenic activity, simulating the effect of magnesium alloy degradation, Acta Biomater. 10 (2014) 2834–2842, https://doi.org/10.1016/j.actbio.2014.02.002.
[103] D.H. Zhu, Y.C. Su, M.L. Young, J. Ma, Y.F. Zheng, L.P. Tang, Biological responses and mechanisms of human bone marrow mesenchymal stem cells to Zn and Mg biomaterials, ACS Appl. Mater. Interfaces 9 (2017) 27453–27461, https://doi.org/10.1021/acsami.7b06654.
[104] X.K. Zhang, Y.L. Zhu, L.Y. Cao, X. Wang, A. Zheng, J. Chang, J.N. Wu, J. Wen, X. Q. Jiang, H.Y. Li, Z.Y. Zhang, Alginate-aker injectable composite hydrogels promoted irregular bone regeneration through stem cell recruitment and osteogenic differentiation, J. Mater. Chem. B 6 (2018) 1951–1964, https://doi.org/10.1039/C7TB03315J.
[105] Z.Y. Peng, C.Q. Wang, C. Liu, H.X. Xu, Y.H. Wang, Y. Liu, Y.T. Hu, J.J. Li, Y.L. Jin, C. Jiang, L.L. Liu, J.S. Guo, L.X. Zhu, 3D printed polycaprolactone/beta-tricalcium phosphate/magnesium peroxide oxygen releasing scaffold enhances osteogenesis and implanted BMSCs survival in repairing the large bone defect, J. Mater. Chem. B 9 (2021) 5698–5710, https://doi.org/10.1039/D1TB00178G.